

An azimuthally resolved study of sloshing cold fronts in three nearby galaxy clustersI-HSUAN LI,¹ SHUTARO UEDA,^{2,3} I-NON CHIU,¹ AND KEIICHI UMETSU⁴¹*Department of Physics, National Cheng Kung University, No.1, University Road, Tainan City 70101, Taiwan*²*Faculty of Mathematics and Physics, Institute of Science and Engineering, Kanazawa University, Kakuma, Kanazawa, Ishikawa, 920-1192, Japan*³*Advanced Research Center for Space Science and Technology (ARC-SAT), Kanazawa University, Kakuma, Kanazawa, Ishikawa, 920-1192, Japan*⁴*Academic Sinica Institute of Astronomy and Astrophysics, 11F of AS/NTU Astronomy-Mathematics Building, No.1, Sec. 4, Roosevelt Road, Taipei 106216, Taiwan***ABSTRACT**

We present a detailed analysis of sloshing cold fronts in a sample of three nearby galaxy clusters (Abell 496, Abell 2029, and Abell 1644) observed with the *Chandra* X-ray Observatory. Cold fronts manifest as sharp edges in the X-ray surface brightness of the intracluster medium (ICM) in galaxy clusters. In the residual X-ray surface brightness maps, where the global ICM distribution has been subtracted, cold fronts generated by gas sloshing are observed at the boundaries of the spiral excesses. We perform a systematic and comprehensive study of the surface brightness edges along the spiral excesses. We find the deficit of the thermal pressure radially inward of the brightness edges, in contrast to stripping cold fronts that typically exhibit higher thermal pressure in brightness edges. Assuming that the sharp edges in the X-ray surface brightness distributions are sustained entirely by the gas bulk motions, we estimate the velocity gradients across the edges that are required to compensate for the deficit of the thermal pressure. We do not find statistically significant velocity gradients along the azimuthal direction. Our results suggest that alternative mechanisms such as magnetic fields and viscosity are necessary to maintain the sharpness of sloshing cold fronts.

Keywords: Galaxy clusters (584) — Intracluster medium (858) — X-ray astronomy (1810)

1. INTRODUCTION

Galaxy clusters, the largest gravitationally collapsed systems in the Universe, accrete their masses by merging with other smaller systems, as well as continuous mass accretion from their surrounding environments. Because the intracluster medium (ICM), which is the diffuse and hot X-ray emitting gas, dominates the baryonic component of galaxy clusters, the mass accretion leaves imprints on the X-ray surface brightness of ICM, such as disturbed morphologies and clumpiness.

High angular-resolution observations performed with the *Chandra* X-ray Observatory have revealed sharp contact discontinuities in the X-ray surface brightness of ICM, recognized as cold fronts or shock fronts (see a complete review in Markevitch & Vikhlinin 2007). Both kinds of fronts are associated with cluster mergers. While shock fronts typically originate from the kinetic energy of major-merger events dissipating in the ICM, cold fronts are considered to be generated by gas

motions at an interface between two phases of the ICM with different entropies. Specifically, a cold front is characterized by a sharp discontinuity across an edge, where the gas on the inner side (typically a remnant core or substructure) has higher density and lower temperature, but maintains the pressure equilibrium with hotter and more diffuse ambient ICM. As the events of major mergers are rare, cold fronts are more frequently detected compared to shock fronts. Given their sharp discontinuities and observability, cold fronts are considered as an ideal place to study the microphysical properties of ICM (Markevitch & Vikhlinin 2007).

Cold fronts are broadly classified into two types: stripping and sloshing cold fronts. Stripping cold fronts are typically observed at the fronts of the collisional gas component of the infalling subclusters (Markevitch et al. 2000; Vikhlinin et al. 2001). When an infalling subcluster hosting a cooler and denser ICM moves through the surrounding gas, a contact discontinuity between two different phases of the gas forms a stripping cold front. For example, stripping cold fronts have been prominently observed in several nearby merging clusters (Hall-

man & Markevitch 2004; Ichinohe et al. 2017; Erdim & Hudaverdi 2019; Ichinohe et al. 2021).

On the other hand, sloshing cold fronts are generated by gas sloshing that is frequently observed in the central region of the cool-core clusters. A widely accepted picture is that minor mergers of substructures with a non-zero impact parameter induce the sloshing motion of the gas (Ascasibar & Markevitch 2006; Roediger et al. 2011; Ichinohe et al. 2015). As the gravitational potential of a cluster is disturbed by the motion of substructures falling into the core, the central ICM gains the angular momentum and hence starts to slosh around the cluster center, leading to the spiral motion of gas observed in an X-ray image.

Observationally, the spiral excess of sloshing cold fronts can be identified in the residual X-ray surface brightness map, from which the global ICM distribution is subtracted (Churazov et al. 2003; Clarke et al. 2004a; Blanton et al. 2011). Sloshing cold fronts typically manifest as multiple concentric arc-shaped discontinuities along the edge of the sloshing spiral, for example, Abell 496 (Ghizzardi et al. 2014) and Abell 85 (Ichinohe et al. 2015). Additionally, the brightness edges of sloshing cold fronts are relatively subtle in contrast to the striking brightness edges observed in stripping cold fronts, leading to challenges in detecting the sloshing pattern. Hence, studies of sloshing cold fronts are still greatly in need to further explore the ICM physics.

The main feature of stripping cold fronts is the significant gradient of the thermal pressure across the X-ray surface brightness edges (Kempner et al. 2002; Rossetti et al. 2007; Ueda & Ichinohe 2024). This phenomenon indicates that the non-thermal pressure substantially contributes to the total pressure support to maintain the sharpness of stripping cold fronts. Similar thermal pressure gradients have also been found in some sloshing cold fronts (Ghizzardi et al. 2014). However, there is also evidence in some galaxy clusters revealing the lack of thermal pressure gradients in sloshing cold fronts (Markevitch et al. 2001; Chen et al. 2017; Paterno-Mahler et al. 2013), indicating the absence of the non-thermal pressure support. Several studies of simulations have shown that the turbulent gas motions, magnetic pressures, and the viscosity of the ICM may be responsible for the non-thermal pressure support (ZuHone et al. 2010; ZuHone 2011; Ichinohe et al. 2019; Gatuzz et al. 2022). Since both stripping and sloshing cold fronts are induced by minor mergers, we would expect the level of the non-thermal pressure support to be similar. Conversely, any inconsistency in the non-thermal pressure support between stripping and sloshing cold fronts may indicate different physical mechanisms. Nowadays, a consensus

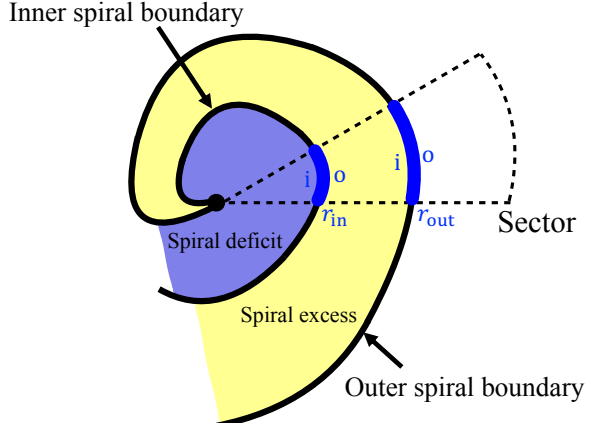


Figure 1. This schematic illustration represents substructures seen in a residual X-ray surface brightness map. The spiral excess (the yellow region) is the primary focus of this work. For each detected surface brightness edge (r_{in} and r_{out}), we denote the side closer to the cluster center with the subscript i , and the farther side with the subscript o . Note that the subscripts “ i ” and “ o ” strictly refer to the radial position relative to the edge. For the outer spiral boundary, the spiral excess lies in region “ i ”, whereas for the inner spiral boundary, the spiral excess lies in region “ o ”.

has not yet been reached on whether stripping and sloshing cold fronts are maintained by the same mechanisms.

Because sloshing gas originates from different regions within a cluster, the microphysical properties of sloshing cold fronts at various positions characterize the gas with different entropies at their initial positions. To this end, azimuthally resolved measurements provide a comprehensive assessment on the mechanism of gas sloshing.

In this work, we carry out an azimuthally resolved study of sloshing cold fronts in three nearby galaxy clusters with prominent surface brightness edges close to the cluster center. Our sample of three clusters includes Abell 496, Abell 2029, and Abell 1644, which are referred to as A496, A2029, and A1644, respectively. With the goal of investigating the thermodynamic properties along the sloshing cold fronts, we azimuthally measure the density and temperature profiles across the X-ray surface brightness edges. Based on these measurements, we further estimate the velocity gradient of the ICM required by the non-thermal pressure support in the detected sloshing cold fronts.

When referring to the sides of the cold front, we use the subscript “ i ” (inner) to denote the region radially inward of the edge (closer to the cluster center) and “ o ” (outer) to denote the region radially outward of the edge. When there are two edges in the same position angle from the cluster center, measurements corresponding to the edge closer to the center are denoted with the sub-

script “in”, while those for the farther edge are denoted with the subscript “out”. We refer to the overdense spiral pattern in the residual X-ray surface brightness map as the spiral excess, and the underdense spiral pattern as the spiral deficit. In this paper, the contrasts of density (j_n), temperature (j_T), thermal pressure (j_p), and entropy (j_K) are defined as the ratios of the quantities measured just radially inward of the X-ray surface brightness edge to those measured just radially outward of the edge, i.e.,

$$j_X \equiv \frac{X_i}{X_o},$$

where $X \in \{n, T, p, K\}$. Figure 1 provides an schematic illustration of a typical sloshing spiral feature, along with the notation adopted in this study.

This paper is organized as follows. A brief summary of previous studies related to the sloshing cold fronts in our sample is provided in Section 2. In Section 3, we describe the method and results of our measurements. We discuss the implications and systematic uncertainties in Section 4. Finally, the conclusions are made in Section 5.

Throughout this paper, we assume a flat Λ CDM cosmology with a Hubble constant of $H_0 = 70 \text{ km s}^{-1} \text{ Mpc}^{-1}$ and a matter density of $\Omega_m = 0.3$. Unless otherwise stated, quoted errors stand for the 68% confidence level (1σ). All positional angles are measured in the counterclockwise direction, from west (0°) to north (90°).

2. SAMPLE AND OBSERVATION DATA

2.1. Sample

We study the three nearby galaxy clusters: A496, A2029, and A1644, within the redshift range $0.03 < z < 0.08$. They are included in the X-ray-selected cluster catalog, known as the HIghest X-ray FLUX Galaxy Cluster Sample (HIFLUGCS; Reiprich & Böhringer 2002). The three clusters are bright and exhibit clearly large excesses of sloshing spirals in their residual X-ray surface brightness maps. Since the spiral excess indicates the presence of the gas sloshing in the plane of the sky, the clear and large spiral excesses in our samples suggest that they are ideal targets to conduct a systematic and azimuthally resolved study. Here, we briefly summarize previous results related to our sample.

A496

A496 is a nearby and bright galaxy cluster ($z = 0.03309$ and $1'' = 0.660 \text{ kpc}$) with a highly symmetric X-ray morphology. With *Chandra* observations, Dupke & White (2003) and Dupke et al. (2007) studied the density and temperature profiles, along with the metal

distribution across the cold fronts, and concluded that the cold fronts in this cluster could be generated by gas sloshing. Tanaka et al. (2006) found the cold front approximately $240''$ south of the cluster center, and estimated the upper limit of the Mach number of the ICM to be ≈ 0.2 . They also suggested that A496 has undergone a merger in the past. Additionally, Ghizzardi et al. (2014) observed that the sloshing spiral has a lower temperature and entropy distribution compared to the ambient gas. Moreover, they observed the thermal pressure gradients of three cold fronts within A496: one between 0° and 30° at a radius of $92''$ away from the cluster center, another between 75° and 120° at a radius of $102''$, and the third between 240° and 285° at a radius of $252''$; each of them was measured with a thermal pressure gradient significantly larger than unity.

A2029

A2029 is one of the most relaxed clusters and located at redshift $z = 0.07872$ ($1'' = 1.488 \text{ kpc}$). Several studies with *Chandra* observations have been done: Based on spectral analyses, Clarke et al. (2004a) suggested that the cooling flow in this cluster is in an early stage. They also discovered extended spiral excesses in the residual X-ray surface brightness map, which are associated with the stripping gas from infalling substructures or gas sloshing motions. Paterno-Mahler et al. (2013) analyzed the northern and southern part of the spiral excesses and obtained smooth thermal pressure profiles in both regions. However, Naor et al. (2020) performed a deprojected analysis of the southwest cold front at $22''$, and found that the thermal pressure radially inward of the cold front is higher than the opposite side at a level of $\approx 1.5\sigma$. In addition, they measured thermal pressure gradients of seven sloshing cold fronts and confirmed the deficit of the thermal pressure on the side with higher density.

A1644

A1644 ($z = 0.04740$ and $1'' = 0.930 \text{ kpc}$) is a postmerging system consisting of two systems: a primary halo (A1644-S) located in the southwest of the sky and a subcluster (A1644-N) in the northeast, each connected by a band of warm gas (Reiprich et al. 2004). Reiprich et al. (2004) compared simulations to observations in X-rays, optical, and radio wavelengths, suggesting that the subcluster has passed through the primary halo. Additionally, Monteiro-Oliveira et al. (2020) measured the physical distance between the two components at 723 kpc . Regarding cold fronts, Johnson et al. (2010) studied the X-ray surface brightness edges in A1644 with *Chandra* observations. They measured the cold fronts in the main cluster (A1644-S) at $12.1''$ in the northeast and

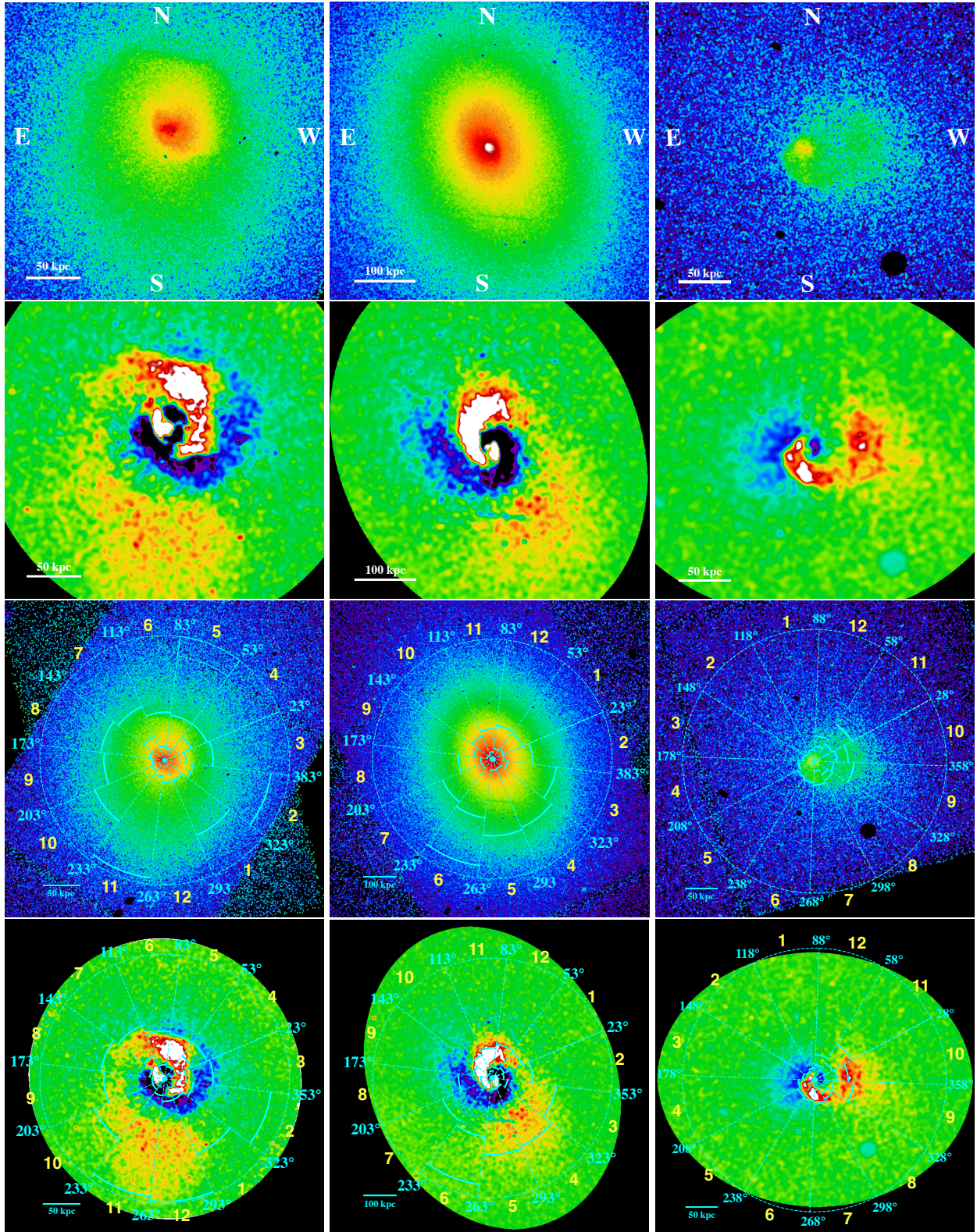


Figure 2. The *Chandra* X-ray surface brightness images (first and third rows) and residual maps (second and fourth rows) of A496 (left), A2029 (middle), and A1644 (right). The zoom-in version of the first and second rows are shown as the third and fourth rows, respectively. The surface brightness images and residual maps are smoothed by a Gaussian kernel with 3 and 10 FWHM, respectively. Point sources and backgrounds are masked by black ellipses in the X-ray surface brightness maps. The bars in the lower-left corner of each panel show the corresponding spatial scales. The numbers in yellow denote the indices of the sectors defined in Table 4. The sectors in cyan with an opening angle of 30° show the regions defined for the azimuthal study. The arcs within the sectors denote the positions of X-ray surface brightness edges, determined by the X-ray surface brightness fitting described in Section 3.2.

32.6'' in the southeast. We only focus on A1644-S in this work, because A1644-N does not exhibit a spiral excess in its residual X-ray surface brightness map. Note that [Johnson et al. \(2010\)](#) studied the cold front in the western region of A1644-N and made the same conclusion.

2.2. Observations and data reduction

We use the archival X-ray datasets of our sample taken with the Advanced CCD Imaging Spectrometer (ACIS; [Garmire et al. 2003](#); [Grant et al. 2024](#)) on board the *Chandra* X-ray Observatory. All datasets are summarized in Table 1. We follow the data reduction process in [Ueda & Ichinohe \(2024\)](#), to which we refer readers for more details. We use the versions of 4.15.1 and 4.10.4 for *Chandra* Interactive Analysis of Observations (CIAO; [Fruscione et al. 2006](#)) and the calibration database (CALDB), respectively. After performing the `lc_clean` task in CIAO to exclude the duration of the flare, we obtain the net exposure time for each cluster summarized in Table 1. Finally, we use `wavdetect` from CIAO to detect and remove point sources.

3. ANALYSES AND RESULTS

In this section, we describe the procedure to detect and analyze the sloshing cold fronts. The detection of the sloshing cold fronts in the residual X-ray surface brightness maps is given in Section 3.1, followed by the fitting of the X-ray surface brightness profiles in Section 3.2. The spectral analyses for the temperature profiles are presented in Section 3.3. Finally, we estimate the thermal pressure and entropy across the detected X-ray surface brightness edges and present the results in Section 3.4.

3.1. The X-ray imaging and the sloshing spirals

The background-subtracted and exposure-corrected X-ray surface brightness images of A496, A2029, and A1644 are shown in the upper panel of Figure 2. These images are taken in 0.5–0.7 keV band. A496 (the upper left panel) and A2029 (the upper middle panel) reveal a clear and highly axial-symmetric morphology in X-rays, suggesting that they are relatively relaxed. In A496, the X-ray surface brightness distribution appears less continuous in the southwest yellow-to-green and the north green-to-blue regions, which is an indication of cold fronts. For A2029, the strip at 85'' south from the X-ray peak is considered to be the X-ray absorption of a foreground edge-on spiral galaxy ([Clarke et al. 2004b](#)). In contrast to the former two clusters, a spiral-like pattern can already be visually identified in the X-ray surface brightness of A1644 (the upper right panel), before making its residual map.

We extract the residual X-ray surface brightness maps to detect the gas sloshing features in our samples, as shown in the lower panel of Figure 2. The residual maps are generated by subtracting an elliptically mean surface brightness distribution from the observed surface brightness map (the upper panel in Figure 2). The parameters characterizing the mean surface brightness elliptical distribution are taken from [Ueda et al. \(2021\)](#), which we summarize them in Table 2. In [Ueda et al. \(2021\)](#), they derived those parameters by using a concentric-ellipse-fitting algorithm ([Ueda et al. 2017](#)) to fit the X-ray surface brightness, with the elliptical model centering at the X-ray brightness peak. Based on these parameters, we evaluate the elliptical model at each position by the mean of its corresponding concentric elliptical ring with a width of 2''. In order to cover the largest *Chandra* observed area, we set the semi-major axes of the models to 252'', 242'', and 222'' for A496, A2029, and A1644, respectively.

We observe large and head-on striking spiral excesses, the feature of gas sloshing, in the residual maps of all samples as seen in second row of Figure 2. We visually identify these spiral excesses, and define their head starting from the brightness excess with the orientation as summarized in Table 3.

We stress that the detection of these spiral excesses is unequivocal even with a different method to create the residual maps—for example, the spirals were also seen in the residual map of A2029 by subtracting a two-dimensional beta model from the image ([Paterno-Mahler et al. 2013](#)). In addition, we observe that the spiral excesses become less distinct after a turn of approximately 180° from their origin, beyond which the spiral excesses become clear again, a feature also seen in [Ghizzardi et al. \(2014\)](#) and [Clarke et al. \(2004a\)](#). The location of these gaps are identified around sectors 8 and 9 in A496, sectors 1 and 2 in A2029, and sectors 8 and 9 in A2029. In [Ghizzardi et al. \(2014\)](#), they suggested that this phenomenon is caused by Kelvin-Helmholtz (KH) instabilities generated by shear flows along the sloshing gas, as confirmed in simulations ([ZuHone et al. 2010](#); [Roediger et al. 2011, 2012, 2013](#)). Another feature is that all three clusters exhibit a pair of spirals with a brightness excess and a corresponding deficit. The white-to-yellow regions in the residual maps represent the excesses of the surface brightness, while the blue-to-black regions represent the deficits. This feature was also found in [Ueda et al. \(2021\)](#), in which they analyzed 28 cool-core clusters, including those in our sample, and showed that all clusters exhibit a pair of over- and under-density patterns in their residual X-ray surface brightness maps.

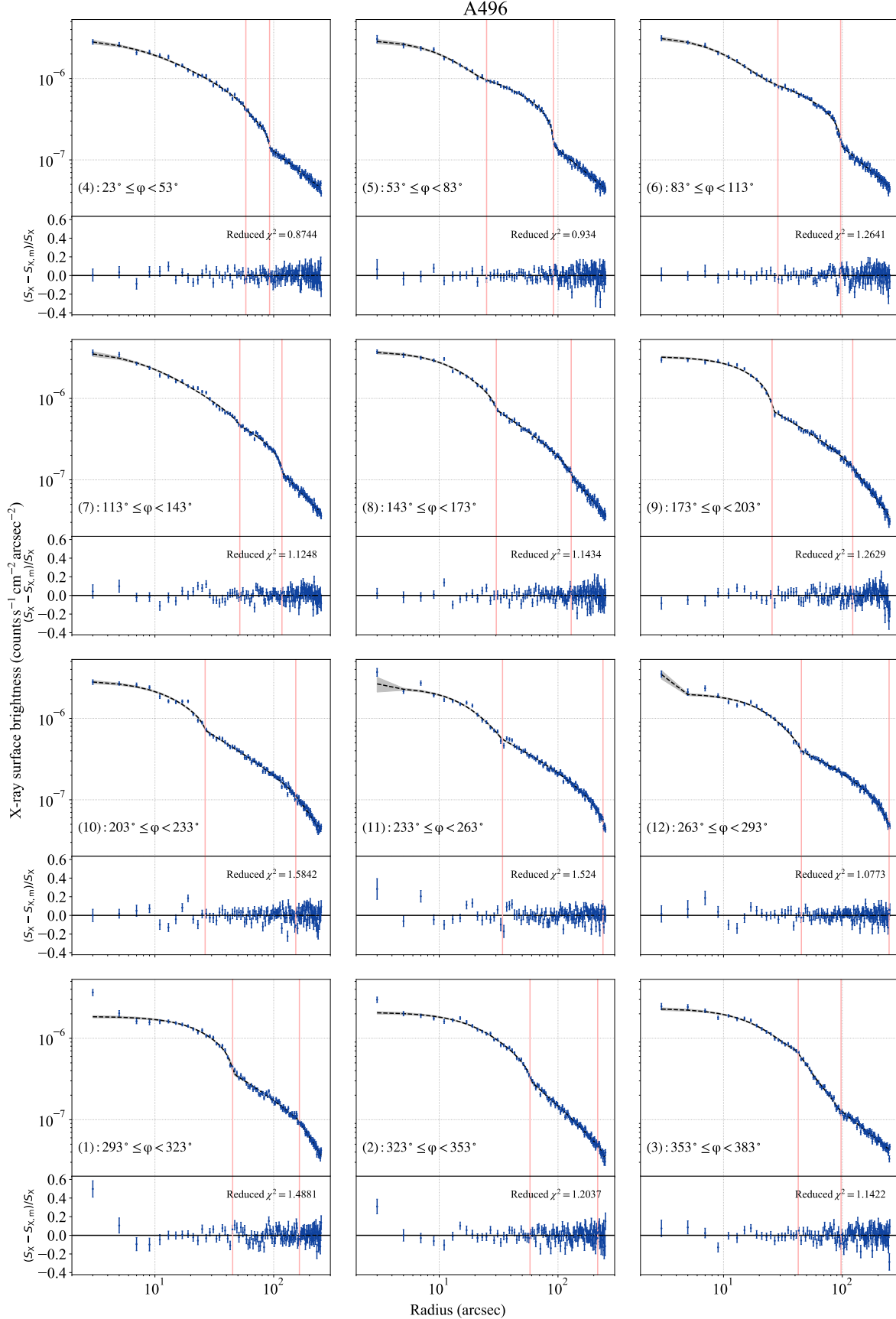


Figure 3. The radial profiles of the X-ray surface brightness extracted from sectors in A496. The blue vertical bars show the 1σ confidence range of the X-ray surface brightness. The black dashed lines show the best-fit X-ray surface brightness profiles. The pink vertical lines denote the best-fit positions of the surface brightness edges (i.e., r_{in} and r_{out}). In addition, the panels below the profiles show the residuals with respect to the best-fit models, computed as $(S_{\text{X}} - S_{\text{X,m}})/S_{\text{X}}$, where S_{X} is the observed surface brightness and $S_{\text{X,m}}$ is the model prediction.

Table 1. Summary of *Chandra* X-ray observations for our sample.

Cluster	Redshift	Physical scale (kpc/")	Expo. time ^a (ks)	ObsID ^b
A496	0.03309	0.660	60.2	3361, 4976, 931
A2029	0.07872	1.488	100.4	4977, 6101, 891
A1644	0.04740	0.930	63.9	2206, 7922

^aTotal net exposure time of *Chandra* observations after masking flare-time intervals.^b*Chandra* observation identification (ObsID) numbers.**Table 2.** Summary of the elliptical model used for generating the residual maps.

Cluster	R.A. ^a	Decl. ^a	PA ^b (deg)	AR ^c	Semi-major axis ("")
A496	04 : 33 : 37.80	-13 : 15 : 40.05	113	0.96	252
A2029	15 : 10 : 56.09	05 : 44 : 41.10	113	0.79	242
A1644	12 : 57 : 11.61	-17 : 24 : 33.09	178	0.81	222

^aSky coordinates (J2000.0) of the X-ray brightness peak.^bPosition angle measured north of west.^cAxis ratio.**Table 3.** Summary of the head of the positive spiral excesses in the residual X-ray surface brightness maps.

Cluster	Azimuthal angle ^a (deg)	Radius ("")	Direction ^b
A496	293	45.13	counterclockwise
A2029	53	25.52	clockwise
A1644	88	19.86	counterclockwise

^aAzimuthal angle measured north of west.^bThe direction for each cluster was chosen based on the winding direction of the spiral excess.

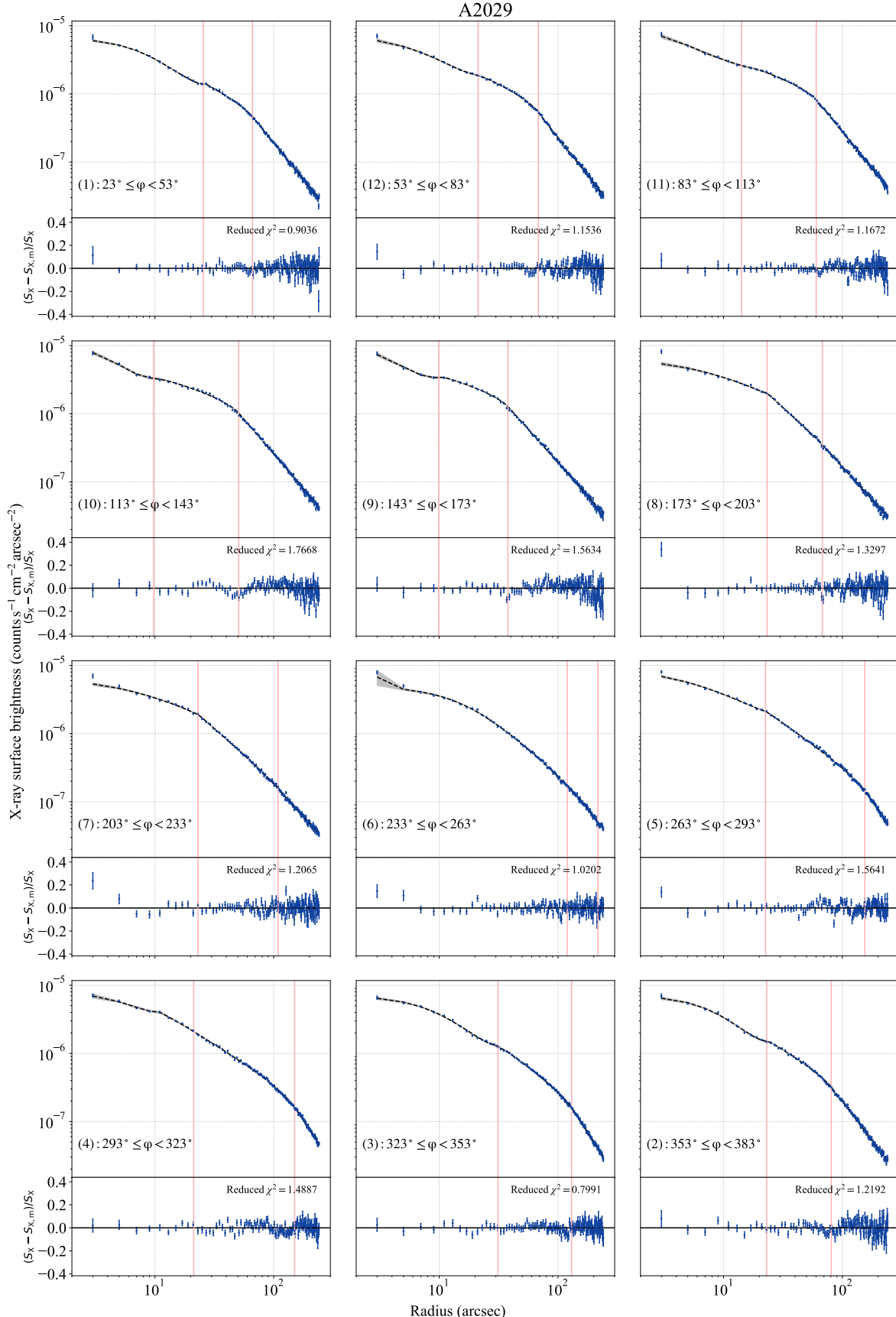


Figure 4. Same as Figure 3, but for A2029.

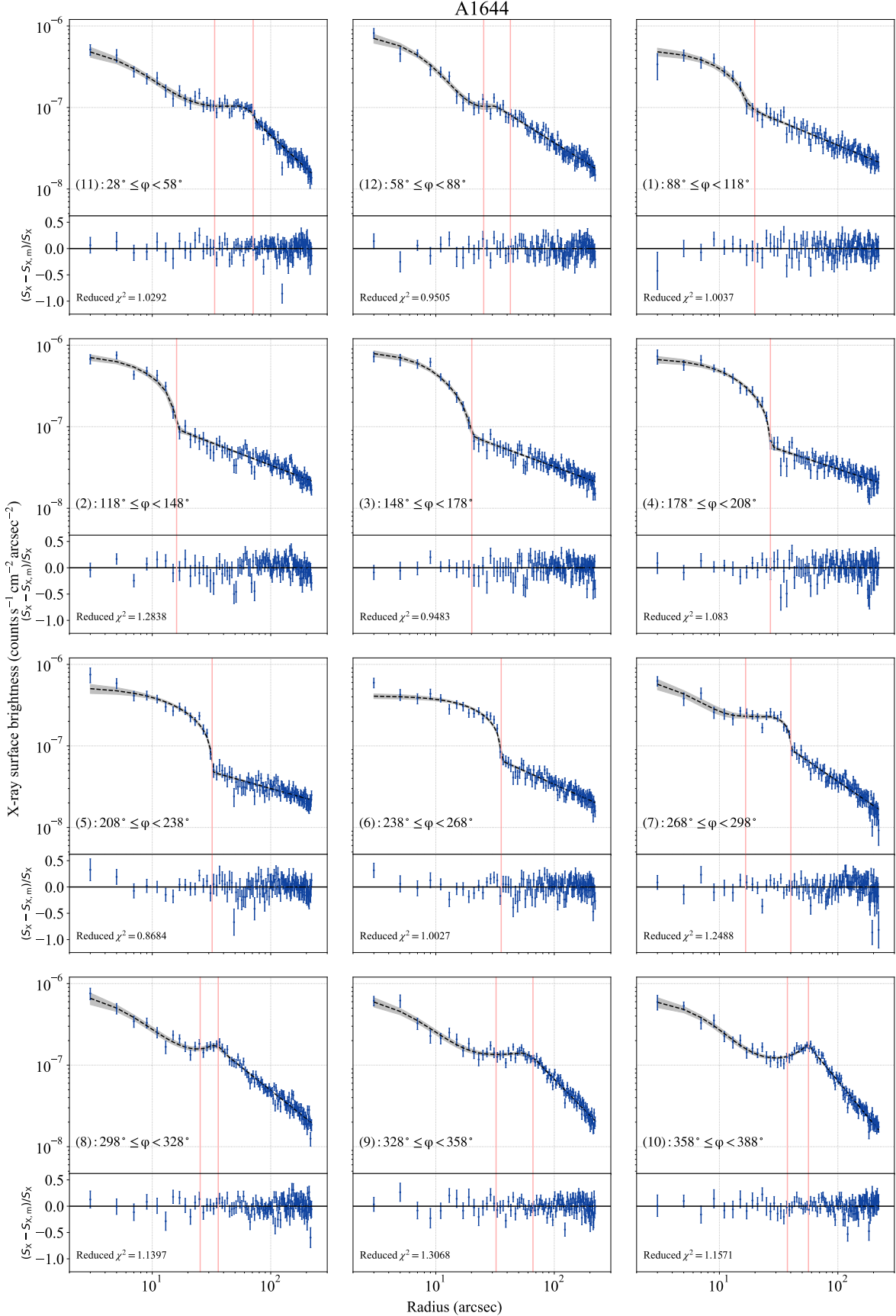


Figure 5. Same as Figure 3, but for A1644.

Table 4. Summary of the azimuthal angle ϕ ranges of the sectors defined in the sample.

Label	A496	A2029	A1644
1	293° – 323°	23° – 53°	88° – 118°
2	323° – 353°	353° – 383°	118° – 148°
3	353° – 383°	323° – 353°	148° – 178°
4	23° – 53°	293° – 323°	178° – 208°
5	53° – 83°	263° – 293°	208° – 238°
6	83° – 113°	233° – 263°	238° – 268°
7	113° – 143°	203° – 233°	268° – 298°
8	143° – 173°	173° – 203°	298° – 328°
9	173° – 203°	143° – 173°	328° – 358°
10	203° – 233°	113° – 143°	358° – 388°
11	233° – 263°	83° – 113°	28° – 58°
12	263° – 293°	53° – 83°	58° – 88°

3.2. The X-ray surface brightness profiles

In this section, we aim to identify the edges in the X-ray surface brightness along the radial direction by using a generalized model. Consider an idealized case of a spiral excess illustrated in Figure 1. At a given positional angle with respect to the spiral head, two edges (r_{in} and r_{out}) are present along the radial direction, except at positional angles aligned with the spiral-head direction. To describe the radial distributions while capturing the edges, we adopt a three-component model, in which the edges are defined at the boundaries between adjacent components. However, due to the noises, the complex morphology of cold fronts, or the parameter degeneracy, the best-fit r_{in} and r_{out} may not well capture the true locations of the pairs of edges. We therefore perform visual inspections to verify the best-fit edge locations. Alternatively, we use a simplified, two-component model when the three-component model fails to provide a good fit.

To analyze the azimuthal variations of the ICM across the sloshing cold fronts, we define 12 sectors with an opening angle of 30° to extract the radial X-ray surface brightness profiles for each cluster. The center of these sectors is set at the X-ray brightness peak of the cluster. We define the position angle of each sector with respect to the elliptical model described in Table 2. The definitions of the sectors are listed in Table 4. Following the same elliptical model, we set the outer boundaries of the sectors in A496, A2029, and A1644 to 252'', 242'', and 222'', respectively. We examine the systematic uncertainties of our measurements by adopting an alternative definition of the sectors, as detailed in Appendix C. The sectors overlaid on the X-ray surface brightness and

residual maps are shown in the third and fourth rows in Figure 2.

In order to measure the density contrast of the X-ray surface brightness edges, we extract the X-ray surface brightness profile of each sector with a radial binning of 2''. Subsequently, all profiles are fitted with either a two- or three-component model integrated along the line of sight. For a uniform analysis, we consistently adopt the three-component model as a starting point for each sector, switching to the two-component model only if the former does not provide a good fit. Importantly, unlike other studies typically done in the literature, our homogeneous and systematic analysis across the sample is a unique strength of this work, avoiding the confirmation bias and reducing the influence of the prior knowledge from our expectation. As a result, our best-fit models provide excellent descriptions of the observed X-ray surface brightness of all sectors in each cluster, as shown in Figures 3, 4, and 5 for A496, A2029, and A1644, respectively.

We describe the models of the density profiles as follows. The three-component model is composed of a beta model for the inner region ($r < r_{\text{in}}$), a first power-law model for the intermediate region ($r_{\text{in}} \leq r < r_{\text{out}}$), and a second power-law model for the outer region ($r > r_{\text{out}}$). This model is expressed as

$$n_e(r) = \begin{cases} n_{e,c} \left[1 + \left(\frac{r}{r_c} \right)^2 \right]^{-3\beta/2} & \text{if } r < r_{\text{in}} \\ \frac{n_{e,r_{\text{in}}}}{j_{n,\text{in}}} \left(\frac{r}{r_{\text{in}}} \right)^{-2s_1} & \text{if } r_{\text{in}} \leq r < r_{\text{out}} \\ \frac{n_{e,r_{\text{out}}}}{j_{n,\text{out}}} \left(\frac{r}{r_{\text{out}}} \right)^{-2s_2} & \text{if } r_{\text{out}} \leq r \end{cases} \quad (1)$$

In Equation (1), $n_{e,c}$ represents the electron number density at the cluster center, and r_c and β are the core radius and slope parameter of the beta model, respectively; meanwhile, $n_{e,r_{\text{in}}}$ ($n_{e,r_{\text{out}}}$) denotes the electron number density at the three-dimensional radius r_{in} (r_{out}) of the inner (outer) X-ray surface brightness edge, and the index s_1 (s_2) corresponds to the slope parameter of the inner (outer) power-law model. By construction, we have $n_{e,r_{\text{in}}} = n_{e,c} \left[1 + (r_{\text{in}}/r_c)^2 \right]^{-3\beta/2}$ and $n_{e,r_{\text{out}}} = n_{e,r_{\text{in}}} / j_{n,\text{in}} \times (r_{\text{out}}/r_{\text{in}})^{-2s_1}$. In such a parameterization, the parameter $j_{n,\text{in}}$ ($j_{n,\text{out}}$) is the density contrast at the radius r_{in} (r_{out}). If $j_n > 1$, the electron number density radially inward of the cold front (i.e., with a smaller distance to the core) is larger than that radially outward, and vice versa. For example, the condition of $j_{n,\text{in}} > 1$ represents a deficit in the density towards a large distance at the edge r_{in} in Equation (1).

If the surface brightness profile of a sector is not well fitted by the three-component model, we adopt a

two-component model instead, which is found to provide a sufficiently accurate fit in this work. The two-component model, which consists of a beta model for the inner profile ($r < r_{\text{in}}$) and a power-law model ($r \geq r_{\text{in}}$) for the outer profile, is described as

$$n_e(r) = \begin{cases} n_{e,c} \left[1 + \left(\frac{r}{r_c} \right)^2 \right]^{-3\beta/2} & \text{if } r < r_{\text{in}} \\ \frac{n_{e,\text{in}}}{j_{n,\text{in}}} \left(\frac{r}{r_{\text{in}}} \right)^{-2s_1} & \text{if } r_{\text{in}} \leq r \end{cases}, \quad (2)$$

where all parameters follow the definitions in Equation (1).

We approximate the X-ray emission using an isothermal model, so that the modelling of the X-ray surface brightness is independent of temperature (e.g., Ichinohe et al. 2017; Ueda & Ichinohe 2024). Additionally, we assume spherical symmetry in the distribution of the ICM, such that the modelling of the X-ray surface brightness profile can be parameterized by a direct integration of $n_e^2(r)$ along the line of sight with a varying normalization. We find the best-fit model of the observed X-ray surface brightness profiles using the affine-invariant Markov chain Monte Carlo sampling (Goodman & Weare 2010) implemented by the `emcee` python package (Foreman-Mackey et al. 2013).

The results of the X-ray surface brightness fitting for A496, A2029, and A1644 are shown in Figures 3, 4, and 5, respectively. Except for the sectors 1 to 6 of A1644, all the profiles extracted from the remaining regions are well-fitted with the three-component model. The fitting results of A496, A2029, and A1644 yield mean reduced χ^2 values of 1.22, 1.27, and 1.09 with the degrees of freedom of 125, 120, 110, respectively.

For a homogeneous study of sloshing cold fronts, we uniformly define the sectors and, hence, they do not align perfectly with the curvature of the edges of the spiral excesses. Despite a uniform analysis, doing so may not accurately capture the density contrasts across the surface brightness edges. Therefore, we investigate the associating systematic uncertainty by additionally analyzing several sectors with the customized directions aligning with the spiral edges (see details in Appendix C). We find that our results are not sensitive to this systematic.

In Figure 6, we show the azimuthal variations of the three-dimensional positions of the edges (r_{in} and r_{out}) and the corresponding density contrasts (j_n). The measurements of the inner and outer surface brightness edges are shown in blue and yellow, respectively. To better examine the azimuthal variations, the data points shown in Figure 6 are plotted starting from the head of the spiral excess, as listed in Table 3, and follow the

direction of the spiral. In the following paragraphs, we present a detailed discussion of each cluster.

A496—As seen in the lower panel of Figure 2, the inner edges of the sectors 1 to 3, and the outer edges of the sectors 4 to 12, are aligned with the outer boundary of the spiral excess, suggesting that the modelling of the X-ray surface brightness correctly captures the sloshing position. Also, as in the upper left panel of Figure 6, the farthest edge is located at $\approx 248''$ from the cluster center in the twelfth sector, indicating that the sloshing cold front could extend to the outskirt of the cluster. For the azimuthal variation of the density contrast (the lower left panel of Figure 6), the mean density contrast j_n of the sharpest edges (r_{out} of the sector 4 to sector 8) is 1.60 ± 0.021 , which is similar to but marginally smaller than density contrasts typically measured in stripping cold fronts (e.g., $1.68^{+0.31}_{-0.23}$ in Abell 3667; Ichinohe et al. 2017). The mean density contrast of the edges along the outer boundary of the spiral excess (i.e., r_{in} in sector 1 to sector 3 and r_{out} in sector 4 to sector 12, by visual inspection) is 1.32 ± 0.028 , similarly indicating a relatively weak contrast. Additionally, we find that the density contrasts at the spiral tail region (the outer edges from sectors 9 to 12) are consistent with unity within 1σ , suggesting no clear density contrast at the spiral-tail region.

A2029—As in the lower middle panel of Figure 2, the inner edges of the sectors 1 to 3 are aligned with the inner boundary of the spiral excess. Meanwhile, the inner edges of the sectors 4, 5, 7, and 8, as well as the outer edges of the sectors 1 to 5 and 9 to 12, are aligned with the outer boundary of the spiral excess. Again, this demonstrates that the robustness of the surface brightness modelling in identifying the sloshing position. The sharpest edges is traced by r_{in} of the sectors 7 and 8 and r_{out} of the sector 9 to sector 11. For sectors 1 to 3, the positions of r_{in} coincide with the inner boundary of the spiral excess, in contrast to the other edges, in which r_{in} is aligned with the outer boundary of the spiral excess. Regarding the values of the density contrasts j_n at the edges that coincide with the outer boundary of the spiral excess, we find that j_n of inner edges in sectors 4, 5, 7, and 8 are significantly below one with their mean density contrast equals to 0.83 ± 0.05 (see Figure 6). This result shows the excess of gas density at the edge of r_{in} , which is opposite to the other two clusters.

A1644—We show the results in the right panel of Figure 6. The striking spiral excess is aligned with the inner edges r_{in} of the sectors 1 to 6 and the outer edges r_{out} of the sector 7, which represent the sharpest edges. These sectors enclose the most clearly visible part of the spiral

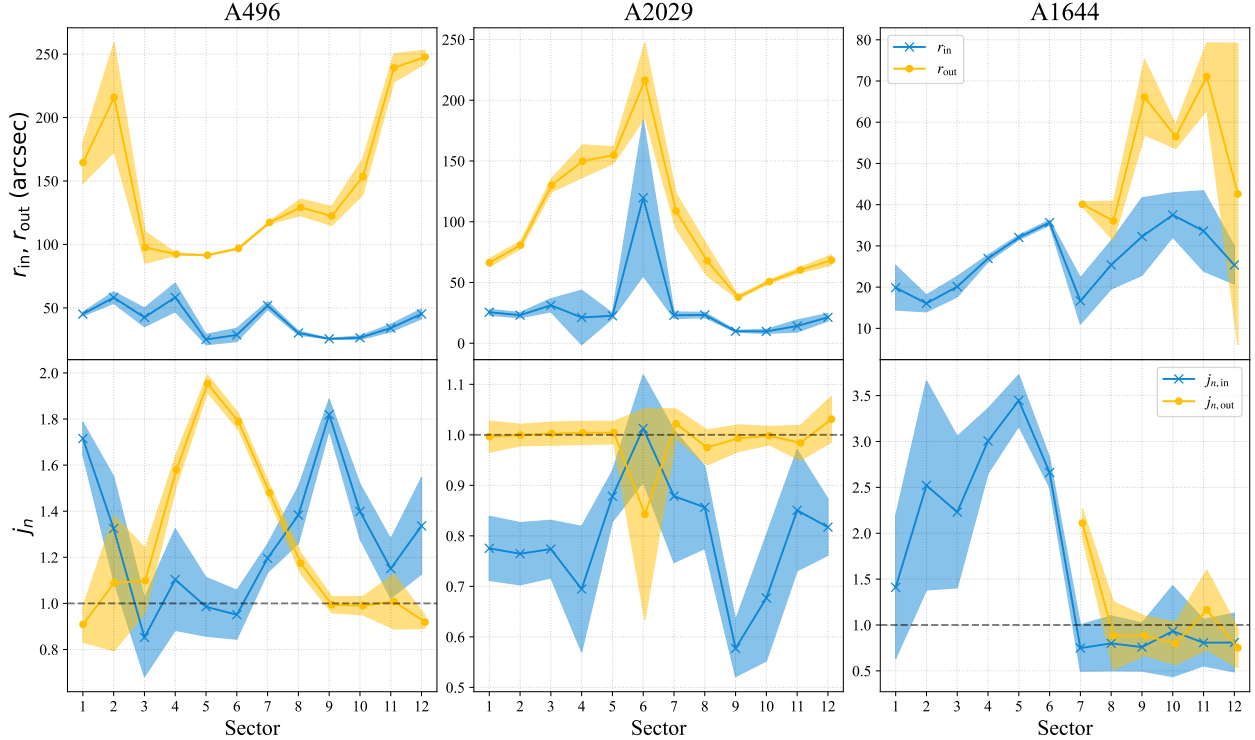


Figure 6. The azimuthal variations of the best-fit three dimensional positions r (top) and density contrasts j_n (bottom) of the X-ray surface brightness edges for A496 (left), A2029 (middle), and A1644 (right), respectively. The blue and yellow data points indicate the best-fit values of the inner and outer detected edges (r_{in} and r_{out}), respectively. The shaded areas represent the 1σ confidence ranges of the best-fit parameters. The horizontal black dashed lines in the bottom panels correspond to unity.

excess in A1644. On the other hand, the sectors 8 to 12 are located at the tail of the spiral excess, such that the surface brightness edges in these sectors are associated with the disturbed morphology of the spiral tail. The mean density contrast (2.48 ± 0.24) of the surface brightness edges along the clearly visible spiral excess is significantly higher than those typically observed in stripping cold fronts (e.g., $j_n = 1.53^{+0.08}_{-0.07}$ in Abell 2554; Erdim & Hudaverdi 2019). It is worth mentioning that the azimuthal variation of the density contrast exhibits a mildly increasing trend along the head of the spiral excess, a feature also observed in stripping cold fronts, where the head exhibits the highest density contrast and then gradually decreases along a tail (Ichinohe et al. 2017).

3.3. X-ray spectral analyses and the ICM temperatures

To measure the temperature contrasts j_T across the detected surface brightness edges (i.e., r_{in} and r_{out}), we divide each sector into several partial-annulus-shaped regions with varying radii from the cluster center, and perform the spectral analyses. For sectors modeled with the two-component model, the position of r_{in} divides

the sector into two components. We define the radial binning of each sector as follows.

A three-component (two-component) model divides a sector into three (two) components by the positions of r_{in} and r_{out} (r_{in}). Beside the positions of r_{in} and r_{out} , we further define radial binning within each component in each sector. Specifically, we adjust the radial binning such that each radial bin contains a comparable number of photon counts. By doing so, we effectively require that the signal-to-noise ratios of individual radial bins in all sectors are consistent within a cluster. For A496 and A2029, the resulting mean X-ray photon counts per radial bin are 1043 and 1537, respectively. On the other hand, the mean photon count for A1644 is lower due to its significantly fainter surface brightness compared to A496 and A2029. For A1644, the resulting radial binning has the mean photon count of 193 for radial bins within the inner component for the two-component sectors, and the inner and intermediate components for the three-component sectors, while in both cases the outer component has a mean of 820. The definitions of radial bins are summarized in Table 5.

Following the procedure described in Ueda & Ichinohe (2024), we use the `specextract` task in CIAO to extract

the individual spectra, responses, and ancillary response files of these radial bins. The spectra for analysis are calibrated using these files to account for instrumental effects. We model the X-ray spectra using **XSPEC** (version 3.0.9; [Arnaud 1996](#)) with the atomic database (version 12.13.0c; [Foster et al. 2023](#)).

As the first step of the spectral analysis, we measure the radial ICM projected temperature profiles for all sectors. Assuming that the ICM is in collisional ionization equilibrium, we fit the **APEC** model ([Smith et al. 2001](#); [Foster et al. 2012](#)) to the X-ray spectra in the energy range between 0.5 keV and 7.0 keV. We fix the column density N_{H} to $4.29 \times 10^{20} \text{ cm}^{-2}$, $3.01 \times 10^{20} \text{ cm}^{-2}$, and $4.17 \times 10^{20} \text{ cm}^{-2}$ for A496, A2029, and A1644, respectively, following the values taken from [HI4PI Collaboration et al. \(2016\)](#). We fix the redshift of the spectra to the cluster redshift. We vary or fix the metal abundances in the spectral models depending on whether we can obtain statistically meaningful constraints from the data. In general, the metal abundance treated as a free parameter for the most radial bins in A496 and A2029 with a few exceptions, for which we refer readers to Appendix B for details. On the other hand, the metal abundance is fixed to 0.3 for A1644 due to the lack of photon counts.

As the second step, after obtaining the projected temperature profiles, we then deproject them to obtain the three-dimensional temperature profiles. The deprojected analyses are performed using the **projct** tool in **XSPEC**, while we fix all parameters of spectra extracted from the outermost radial bins to the best-fit values obtained from the projected spectral analyses. The metal abundances of individual radial bins are assigned based on the average metal abundance of the density component to which each radial bin belongs, with the component determined from the density model described in equations (1) and (2).

The radial projected and deprojected temperature profiles are shown as orange and blue data points in Figure 7, 8, and 9 for A496, A2029, and A1644, respectively. These profiles clearly show that these clusters are cool-core systems, with temperatures gradually decreasing towards the cluster center.

We present the azimuthal variations of the deprojected temperature contrasts j_T across the X-ray surface brightness edges in Figure 10. Considering the azimuthal variations of j_T along the sharpest edges described in Section 3.2, the strongest temperature contrasts occur at the middle sections of the spiral excesses, with mean temperature contrasts of $0.98^{+0.11}_{-0.083}$, $0.67^{+0.18}_{-0.10}$, and $0.31^{+0.054}_{-0.031}$ for A496, A2029, and A1644. We note that the temperature contrast j_T in A1644

is most prominent, consistent with its density contrast j_n , indicating that the gas radially inward and outward of the surface brightness edges has significantly distinct thermodynamic properties. Additionally, a similar trend in the azimuthal variation is also found in stripping cold fronts, where the temperature contrast typically peaks at the leading edge of the front.

For sloshing cold fronts, the gas within the spiral excess is expected to be colder than the surrounding ambient gas. In this picture, we expect $j_T > 1$ and $j_T < 1$ at r_{in} and r_{out} , respectively. There are some edges that yield $j_T > 1.0$ at a 1σ level. We visually inspect the positions of these edges in the residual maps (the bottom panel in Figure 2) and conclude that there are three types of feature that could result in the super-unity temperature contrast: (1) The positions of the detected edges are not aligned with the boundaries of the spiral excesses, such as r_{out} of the sector 1 in A496, r_{in} of the sector 6 and r_{out} of the sector 7 in A2029, and r_{out} of the sector 10 in A1644; (2) The edges are located along the inner boundaries of the spiral excesses, where j_T is expected to be higher than unity, for example r_{in} of the sector 6 in A496 and r_{in} in sector 11 in A2029 (3) The edge lies at the outer boundary of the spiral deficit, where the gas is warmer and less dense than its surroundings. In this configuration, the contacting surface is also expected to have $j_T > 1.0$, as in r_{out} of the sector 8 in A2029. Overall, these three cases are all attributed to the imperfect detection of the positions of the surface brightness edges.

3.4. The thermal pressures and entropy

In this section, we derive the azimuthal profiles of the thermal pressure contrasts j_p , defined as the ratio of the thermal pressure radially inward of the surface brightness edge (p_i) to that radially outward of the edge (p_o). The thermal pressure is expressed as

$$p = n_e \times T, \quad (3)$$

where n_e represents the ICM electron number density and T is the deprojected ICM temperature.

The azimuthal variations of thermal pressure contrasts j_p of the sample are shown in Figure 10. When focusing on the sharpest edges described in Section 3.2, we find that the thermal pressure contrast is less prominent at the middle sector (sector 5) and j_p are generally above unity in A496. In contrast, both A2029 and A1644 exhibit a distinct feature with A496, characterized by the strongest thermal pressure contrast appearing in the middle sector and remaining below one. The findings of sub-unity pressure contrasts at the outer boundaries of the spiral excesses suggest that the sloshing ICM contributes substantial non-thermal pressure

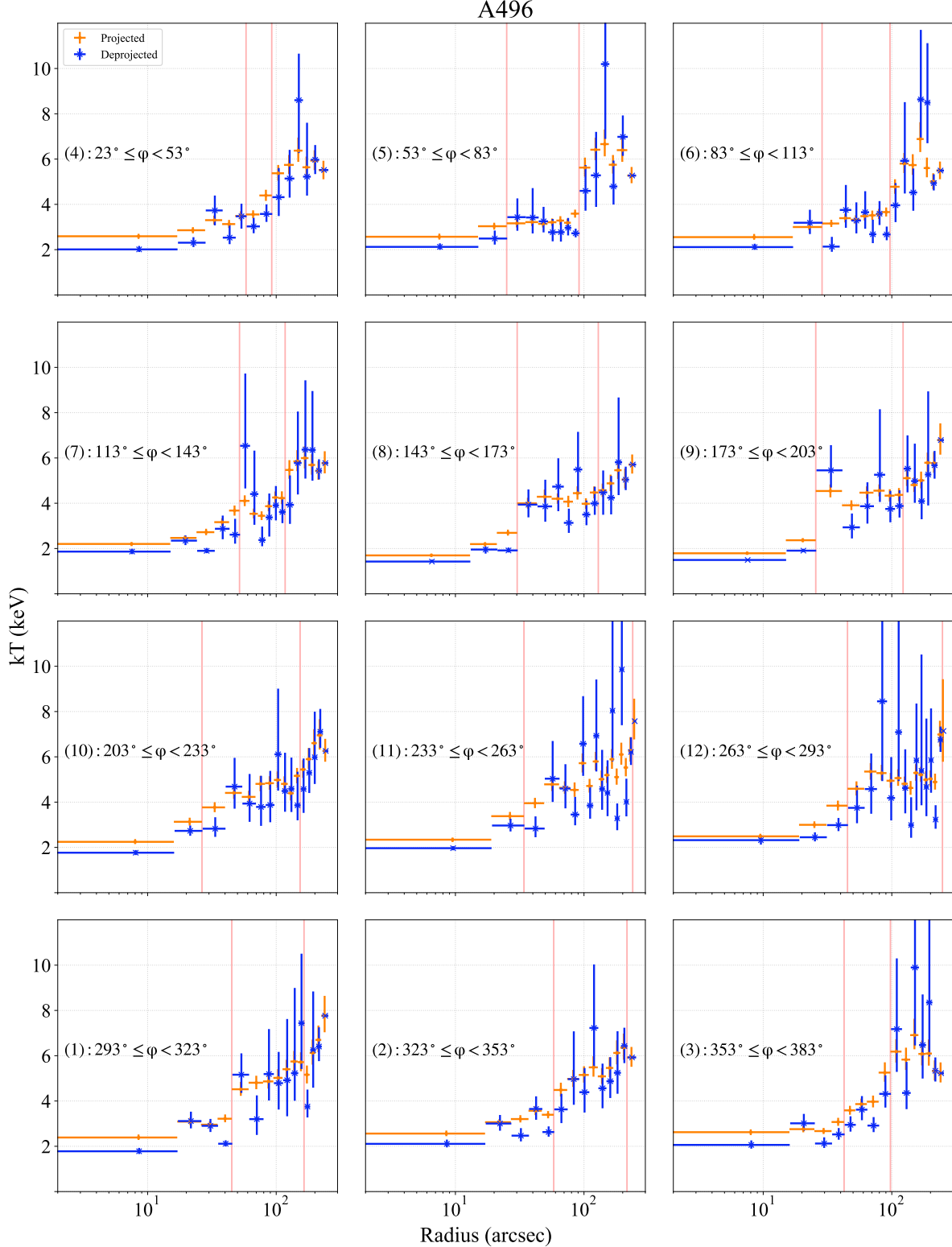


Figure 7. Radial ICM temperature profiles of each sector in A496. The orange and blue data points show the projected and deprojected temperature, respectively. The horizontal bars represent the ranges of the radial bins and the vertical bars denote the 1σ confidence range of the temperature. The pink vertical lines show the positions of r_{in} and r_{out} described in Section 3.2.

support to the cold fronts, in agreement with simula-

tions (ZuHone et al. 2013). Furthermore, the distinct

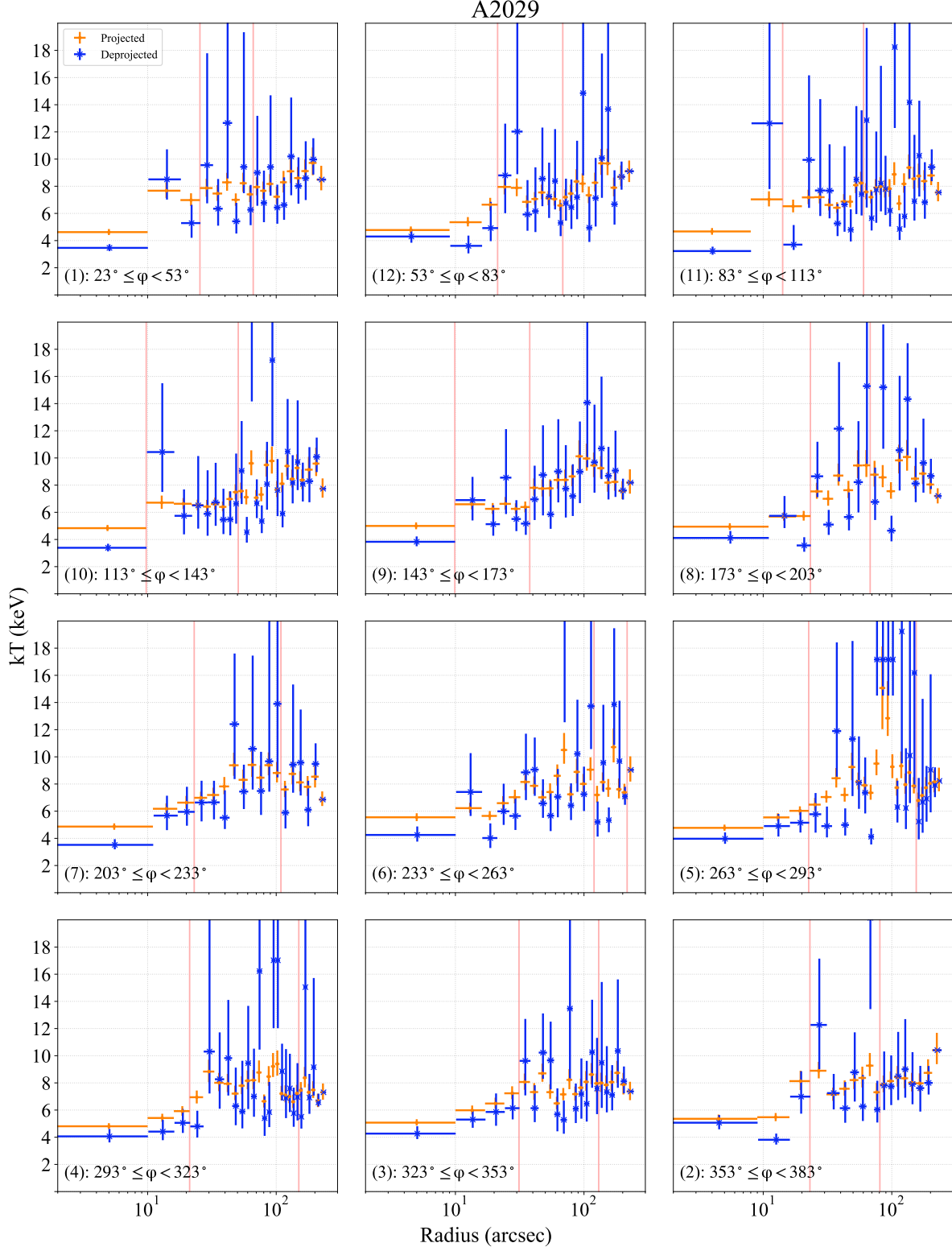


Figure 8. Same as Figure 7, but for A2029.

azimuthal variations of the thermal pressure contrasts in our sample relative to those in stripping cold fronts

(Ueda & Ichinohe 2024) suggest that these two types of

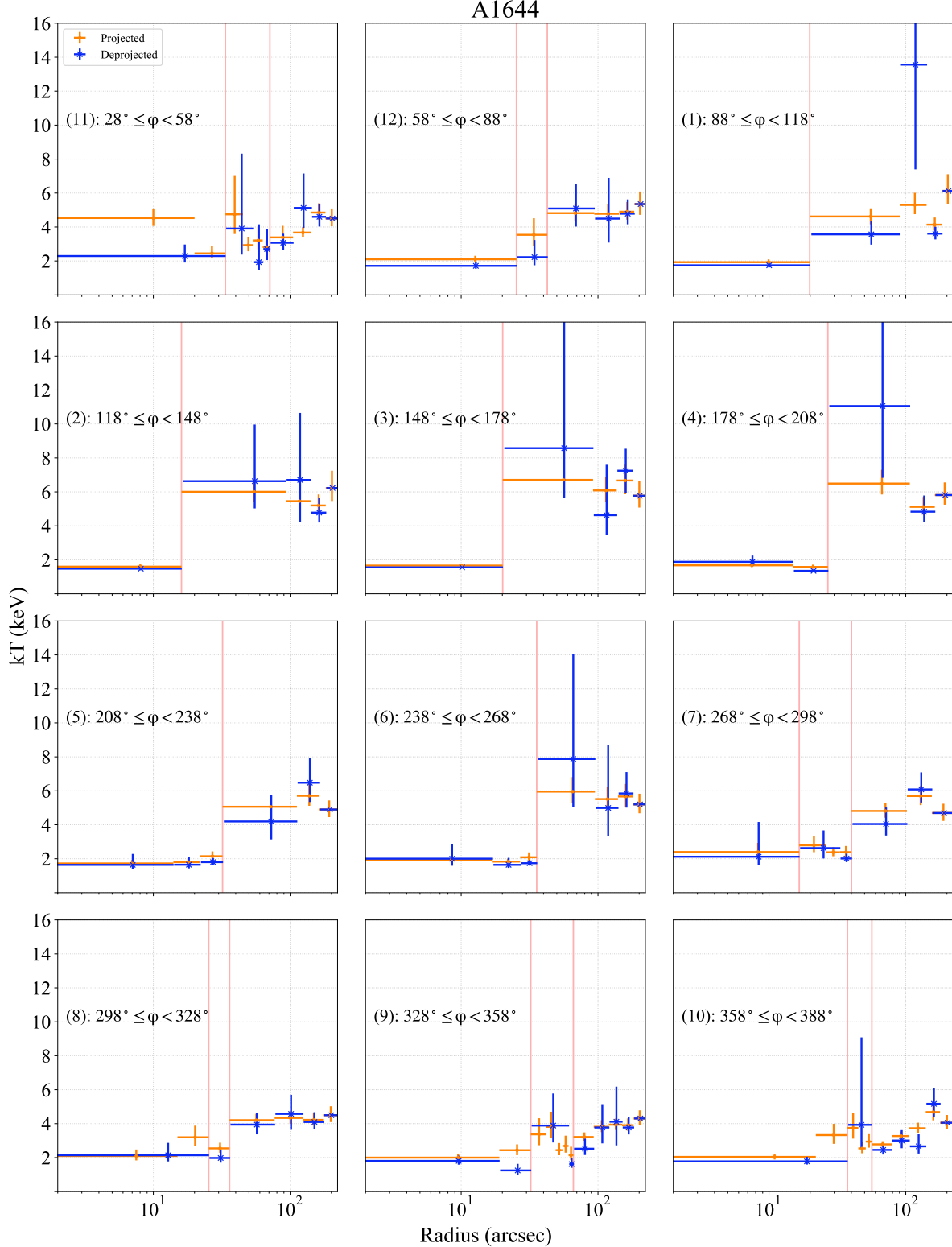


Figure 9. Same as Figure 7, but for A1644.

cold fronts are supported by different physical mechanisms.

For reference, we derive the entropy, which is computed as

$$K = n_e^{-2/3} \times T. \quad (4)$$



Figure 10. The azimuthal variations of the deprojected temperature contrasts, pressure contrasts, entropy contrasts, and the velocity gradients (from top to bottom) across X-ray surface brightness edges for A496 (left), A2029 (middle), and A1644 (right), respectively. The blue and yellow data points indicate the contrasts at r_{in} and r_{out} , respectively. The shaded areas represent the 1σ confidence ranges of contrasts. The horizontal black dashed lines correspond to unity or zero (bottom panel).

Similarly, we present the azimuthal variations of entropy contrasts j_K defined as the entropy radially inward of

the surface brightness edge divided by that radially outward of them ($\frac{K_i}{K_o}$), in Figure 10.

In the body of a sloshing spiral, where the ICM temperature is relatively low, we expect that the temperature contrast j_T is larger (smaller) than unity at the inner (outer) spiral boundary of the spiral excess. Similarly, we expect the density contrast j_n is smaller (larger) than unity at the inner (outer) spiral boundary, because the ICM density is higher in the spiral excess of a sloshing spiral. As a result, the entropy contrast j_K of a sloshing cold front is expected to have $j_K > 1$ ($j_K < 1$) at the inner (outer) spiral boundary. For each cluster in our sample, the entropy contrasts on the sharpest edges aligned with the outer boundaries of the spiral excesses (listed in Section 3.2) are largely smaller than 1, with A1644 showing the most significant entropy contrast ($j_K = 0.18^{+0.04}_{-0.03}$). In the profile of A2029, however, the entropy contrasts across the outer edges r_{out} at the outer boundary of the spiral tail (sectors 1 to 4) are broadly consistent with unity; meanwhile, its thermodynamic properties of the ICM radially inward and radially outward of the edges differ only slightly in the tail region. We note that the entropy contrast depends more strongly on the temperature contrast than the density contrast, because the latter enters with a power of $-2/3$ and the former scales linearly in the entropy.

4. DISCUSSION

In Section 4.1, we present the detected X-ray surface brightness edges that satisfy the criteria of cold fronts. We discuss the velocity gradients as the indicator of the non-thermal pressure supports for sloshing cold fronts in Section 4.2.

4.1. Sloshing Cold fronts in the sample

In this section, we describe the criteria of detecting a sloshing cold front in our cluster sample. Because the density and temperature contrasts of a sloshing cold front are typically less prominent than those of stripping cold fronts, we adopt a relatively loose criterion for identifying sloshing cold fronts given the same data. In this work, a cold front is identified as the X-ray surface brightness edges with both

$$j_n > 1 \text{ and } j_T < 1$$

at greater than a 1σ confidence level. Although sloshing cold fronts may occur along either the inner or outer boundaries of the spiral excess, the inner boundary lies too close to the cluster center to be identified given the angular-resolution limits of observations. Additionally, the central region often exhibits strong perturbations that obscure the surface brightness edges. For these reasons, we only consider the edges aligned with the outer boundaries of the spiral excess. Since the gas within

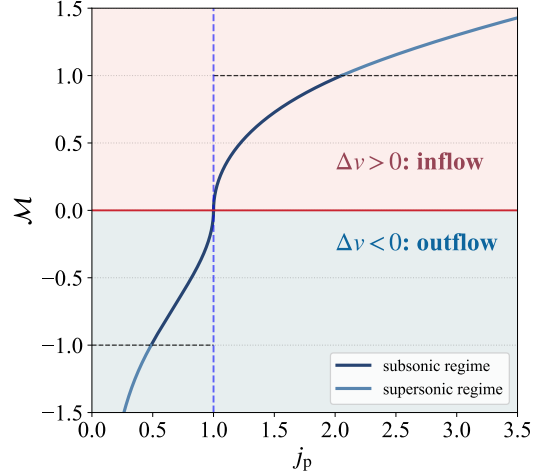


Figure 11. The relation between the thermal pressure contrast j_p and the Mach number M as defined by Equation (5). The horizontal dashed lines at $M = 1.0$ and $M = -1.0$ separate the plot into two regions: subsonic region, corresponding to $|M| \leq 1$, and supersonic region, corresponding to $|M| > 1$.

a spiral excess is expected to share the same physical properties, excluding the edges along the inner spiral boundary does not alter our physical interpretation, and therefore considering only the edges at the outer spiral boundary yields equivalent results.

In this definition, we identify the cold fronts at r_{in} in sector 1 and 2 and r_{out} in sector 5 and 6 in A496. The cold fronts in sector 1 and 2 are newly discovered, whereas those in sector 5 and 6 have been reported previously (Ghizzardi et al. 2014).

For A2029, we do not detect sloshing cold fronts at statistically significance levels under our criterion, even there are clear spiral excesses in the surface brightness, temperature or entropy maps. This picture is consistent with all previous work (Clarke et al. 2004b,a; Paterno-Mahler et al. 2013), suggesting that either sloshing cold fronts genuinely do not exist in the observed spiral excesses or that X-ray observations with higher resolution will be needed for this cluster.

In A1644, we detect cold fronts at r_{in} from sector 2 to sector 6 and at r_{out} in sector 7, which are consistent with the result in Johnson et al. (2010).

4.2. The velocity gradients

In Section 3.4, we observe the contrasts of the thermal pressure at the X-ray surface brightness edges (see Figure 10), strongly indicating the presence of non-thermal pressure supports to maintain the sharpness of the cold fronts. In fact, stripping cold fronts in nearby galaxy clusters have been studied in this context (e.g.,

Vikhlinin et al. 2001; Ichinohe et al. 2017; Ueda & Ichinohe 2024). As follows, we discuss the source of the non-thermal pressure support in the observed sloshing cold fronts.

If the ram pressure of the ICM bulk motion is the dominant component for the non-thermal pressure support, we are able to infer the velocity gradients (Δv) of the ICM across the surface brightness edges from the thermal pressure contrasts (j_p).

Approximate the ICM flow as a free stream across the edge. We define the sign of the velocity to be positive toward the cluster center. Following Landau & Lifshitz (1959) and Vikhlinin et al. (2001), the relation associating the thermal pressure contrast with the ICM Mach number \mathcal{M} is expressed as

$$j_p = \begin{cases} \left(1 + \frac{\gamma-1}{2}\mathcal{M}^2\right)^{\frac{\gamma}{\gamma-1}} & \text{if } \mathcal{M} \leq 1 \\ \left(\frac{\gamma+1}{2}\right)^{\frac{\gamma+1}{\gamma-1}} \mathcal{M}^2 \left(\gamma - \frac{\gamma-1}{2\mathcal{M}^2}\right)^{\frac{-1}{\gamma-1}} & \text{if } \mathcal{M} > 1 \end{cases}, \quad (5)$$

where the adiabatic index of the monatomic gas γ is set to 5/3, and \mathcal{M} is the Mach number of the gas flow across the edges toward the center. By construction, we have $\Delta v \equiv v_o - v_i$, where v_o and v_i are the velocities of the gas bulk motion radially outward and radially inward of the edge, respectively. In this notation, an inflow (outflow) has $\Delta v > 0$ ($\Delta v < 0$). The velocity gradient Δv across the surface brightness edges is related to the Mach number \mathcal{M} as

$$\Delta v = v_o - v_i = \begin{cases} -\mathcal{M} \times c_{s,i} & j_p < 1 \\ \mathcal{M} \times c_{s,o} & j_p \geq 1 \end{cases}, \quad (6)$$

in which c_s is the sound speed of the free-streaming gas of on the lower thermal pressure side. We compute the sound speed as $c_s = (\gamma T / m_p \mu)^{1/2}$, where m_p is the proton mass, and the mean molecular weight of the ICM μ is set to 0.6. We show the relation between the thermal pressure contrast and the Mach number in Figure 11.

The physical picture is as follows. If the pressure contrast at the edge is greater than one ($j_p \geq 1$), implying that the thermal pressure radially inward of the front is higher, the gas radially outward of the front is required to move toward the cluster center to maintain the pressure equilibrium if the non-thermal pressure entirely arises from the gas bulk motion. This leads to an inflow of the gas bulk motion. Conversely, if the pressure contrast is lower than unity, the bulk motion of the gas results in an outflow at the edge of the front.

We calculate the azimuthal variations of the velocity gradients as in Figure 10. For the sharpest edges in A496, the velocity gradients Δv are generally consistent across sectors, showing no clear azimuthal trend. The

ICM velocities radially inward of the edges v_i are lower, in contrast to simulation results, which predict that the turbulent velocity within the spiral excess region is higher than the ambient ICM (ZuHone et al. 2013). In A2029, the velocities radially inward of the edges v_i are higher, and the velocity gradients Δv gradually increase along the sectors toward the tail region. For A1644, the amplitude of velocity gradients $|\Delta v|$ along the sharpest edges remains nearly constant, and the velocities radially inward of the edges v_i are generally higher, except at r_{in} in sector 5 and r_{out} in sector 7, where $v_i < v_o$.

Azimuthally resolved studies of stripping cold fronts indicate that the highest thermal pressure contrasts exist at the leading edge of the cold front (Ichinohe et al. 2017; Ueda & Ichinohe 2024), which is due to the highest velocity gradient generated by the bulk motion of the infalling merging subcluster. On the contrary, the azimuthal variations of velocity gradients observed in our sample vary from cluster to cluster, strongly suggesting that the bulk motion of the sloshing spiral excess may not be the primary source of the non-thermal pressure support for sloshing cold fronts.

One of the possible mechanisms for the non-thermal pressure support, apart from the ICM bulk motions, is the ICM microphysical properties, such as turbulences, magnetic fields, viscosity, and tangential gas flows. The tangential flow of the ICM is expected to be the fastest and highly ordered at the starting position of the spiral excess. This highly ordered flow stretches the magnetic field along the flow direction, which is capable of supporting cold fronts.

Indeed, it was discovered in MeerKAT observations that radio jets bent by magnetic fields align well with the structure of a cold front in the merging cluster Abell 3376 (Chibueze et al. 2021). Furthermore, Walker et al. (2017) found that radio mini-halos in the cool cores of galaxy clusters exhibit morphologies similar to the corresponding cold fronts observed in X-rays. The radio emissions are produced by the synchrotron emission of electrons which are re-accelerated as turbulence in the sloshing motions. These features suggest that magnetic fields might play a role in shaping sloshing cold fronts, resulting in non-negligible magnetic pressures. It is noteworthy that simulations from ZuHone et al. (2013) found that the turbulent motion of the sloshing ICM is amplified, resulting in significantly higher turbulent velocities compared to that of the ambient ICM. This suggests a noticeable contribution from the turbulent motion of the ICM to the non-thermal pressure support in sloshing cold fronts.

We stress that the velocity gradient estimated in this work relies on an estimate from the thermal pressure

contrast, under the assumption that all non-thermal pressure support arises from the bulk motion of ICM, as in stripping cold fronts. In sloshing cold fronts, however, the ICM turbulent motion could be attributed to the velocity gradient we observed. Since the gas motion may not be the only source of the non-thermal pressure, our result can be considered as an upper limit on the velocity of the bulk motion. To this end, the ongoing X-ray observatory *XRISM* (Tashiro et al. 2024) with high-resolution spectroscopy will enable us to directly measure the ICM motions to further explore the source of the non-thermal pressure support in sloshing cold fronts.

5. CONCLUSIONS

In this paper, we perform a systematic and azimuthally resolved study of the sloshing cold fronts observed with *Chandra* in galaxy clusters A496, A2029, and A1644. These clusters are X-ray bright at low redshift ($z \lesssim 0.08$) with the gas sloshing pattern lying in the plane of sky, suggesting an ideal sample for an azimuthal study of cold fronts.

For each cluster, we identify the locations of the edges of the sloshing cold fronts in the residual X-ray surface brightness map, which is obtained by subtracting an elliptical mean model from the global observed X-ray emission. All three clusters show clear spiral excesses in the residual maps. For each cluster, we define twelve sectors, each with an open angle of 30° , starting from the head of the sloshing spiral excess. We consistently fit a two- or three-component model to the observed X-ray surface brightness profile of each sector. The edge locations of the sloshing cold fronts are inferred by the resulting multi-component models.

For each sector of the clusters, we measure the X-ray temperature profile using radial bins with equal photon counts. We estimate the deprojected temperature profile using a de-projected technique assuming spherical symmetry. With the deprojected temperature profiles, we derive the azimuthal and radial distributions of the thermal pressure and entropy. As a result, we obtain the jumps across the sloshing edges along the azimuthal direction in the ICM density, temperature, thermal pressure, and entropy, which are denoted as j_n , j_T , j_p , and j_K , respectively. Assuming that the non-thermal pressure support is dominated by ICM bulk motions, we estimate the velocity gradients using the Mach number derived from the thermal pressure contrast j_p .

For these three clusters, we find the following conclusions:

- Based on the criteria that both the density and temperature contrasts deviate from unity by more than 1σ , we identify new cold fronts in sectors 1 and 2 ($293^\circ \leq \phi < 353^\circ$) in A496. In addition, our cold front measurements in A496 show no statistically significant discrepancies compared with previous work. We confirm the absence of cold fronts in A2029. For A1644, we recover the previously reported cold fronts, while our analyses adopt a more refined definition of the sectors.
- For our sample, the pressure contrasts j_p across the edges are mostly less than 1, suggesting the presence of the non-thermal pressure support radially inward of the edges (i.e., on the side closer to the cluster center) to maintain the sharpness of the edges.
- The azimuthal variations of the velocity gradients across the spiral edges significantly differ from those obtained in stripping cold fronts, in which the pressure equilibrium is mostly maintained by the ICM bulk motion. Our results imply a source other than the gas bulk motion for the non-thermal pressure support in the sloshing cold front. We discuss alternative mechanisms for the non-thermal pressure support in sloshing cold fronts, such as magnetic fields, viscosity, or turbulence in the ICM.

We examine the systematic uncertainties associated with the definitions of the sectors, by performing the identical analyses in the sectors that are tailored to fit the curvature of the observed spiral excesses. We find statistically consistent results and therefore conclude that our results are not significantly affected by the definition of the azimuthal binning.

We present a full azimuthal analysis of the clusters A496, A2029, and A1644, including detailed measurements of thermal contrasts across the surface brightness edges. Furthermore, our results indicate the necessity of the non-thermal pressure support in sloshing cold fronts, which suggests a different mechanism to that of stripping cold fronts. This work paves a way forward for studies using the ongoing X-ray mission *XRISM*, which enables high-resolution X-ray spectra to uncover the velocity structure and dynamical state of ICM cold fronts.

ACKNOWLEDGMENTS

This work is supported by the National Science and Technology Council in Taiwan (Grant NSTC 111-2112-M-006-037-MY3 and 114-2112-M-006-017-MY3). We

thank Sheng-Chieh Lin for providing constructive comments on this manuscript. I-Hsuan Li thanks the support from the ASIAA Summer Student Program. I-Non Chiu thanks Yi Yang for the hospitality in the Institute of Physics (IoP), Academia Sinica. This work is supported by JSPS KAKENHI grant number JP25K23398 (S.U.). Shutaro Ueda acknowledges support by Program for Forming Japan’s Peak Research Universities (J-PEAKS) Grant Number JPJS00420230006. K.U. acknowledges support from the National Science and Technology Council of Taiwan (grant NSTC 112-2112-M001-027-MY3) and the Academia Sinica Investigator Award (grant AS-IA112-M04). The scientific results in this article are based on data obtained from the Chandra Data Archive (CDA).

Facilities: CXO

Software: astropy ([Astropy Collaboration et al. 2013](#)), CIAO ([Fruscione et al. 2006](#)), XSPEC ([Arnaud 1996](#))

APPENDIX

A. RADIAL BINNING DEFINITION

Table 5 summarizes the radial bins adopted in the spectral analyses.

B. METAL ABUNDANCE IN PROJECTED SPECTRAL ANALYSES AND TIED RADIAL BINS IN THE DEPROJECTED SPECTRAL ANALYSIS

The metal abundance are treated as free parameters for the most radial bins in A496 and A2029. A few exceptions are made, where the abundances of spectra from the radial bins listed in the Table 6 are set to the mean of the adjacent radial bins. In addition, for the outermost radial bin of the sector 17 in A496 and sector 2 in A2029, the metal abundances are fixed to the mean values of the outermost radial bins from other sectors within the same cluster. On the other hand, the metal abundances of spectra extracted from A1644 are set to 0.3, because we cannot put any statistically meaningful constraints for this cluster with a free parameter of the abundance. The radial ICM metal abundance profiles of A496 and A2029 are shown in Figure 12 and 13, respectively. Because the photon counts per bin in A1644 are insufficient to statistically constrain the deprojected temperature, we tied several adjacent radial bins together to analyze this cluster. The combined bin groups are listed in Table 7.

C. SYSTEMATIC UNCERTAINTY OF THE SECTOR DEFINITION

In our analyses, we set the X-ray brightness peak as the geometric center of the sector. However, defining the sectors along the curvature of spiral excess might improve the measurements of density and temperature contrasts. To investigate systematic uncertainties resulting from our sector definition, we additionally analyze several X-ray surface brightness profiles extracted from the sectors defined along the curvature of the spiral excess. Finally, we estimate the differences in density contrasts j_n between our fiducial results and those defined along the curvature of the spiral excess, and compare them with previously published studies.

A496

According to the *XMM-Newton* observation conducted by Ghizzardi et al. (2014), a sharp cold front with a boxy morphology is located $30.8''$ (20 kpc) northwest of the cluster center. We therefore define a sector centering at (4:33:38.4614, -13:15:18.242), scanning from 0°

to 30° , with a radial range of $32'' - 252''$. The curvature of this sector aligns with the southern part of the boxy morphology in the residual X-ray surface brightness map of A496, as shown in the left panel of Figure 14. For this sector, We marginally detect a surface brightness edge at $89.5 \pm 12.9''$ from the center of the sector, with a density contrast of $j_n = 1.30 \pm 0.25$ and a temperature contrast of $j_T = 0.64^{+0.13}_{-0.10}$, which yield a thermal pressure contrast of $j_p = 0.83^{+0.23}_{-0.21}$. Given that the pressure contrast of the sector 4, defined in Section 3.2 and largely overlapping with the new sector, is $j_p = 1.31^{+0.42}_{-0.29}$, the difference in pressure contrast between the two sectors is 1.1σ . This indicates that the two measurements are statistically consistent, supporting the reliability of the fiducial sector definition.

Another sloshing cold front with the observation from *XMM-Newton* is situated at $\approx 246.154''$ (160 kpc) from the cluster center, within the azimuthal angle range of 240° to 285° (Ghizzardi et al. 2014). Since this cold front lies close to the outer boundaries of the sector 11 and sector 12, we analyze X-ray surface brightness profiles extracted from sectors defined by extending the outer boundaries of the sector 11 and sector 12 to a radius of $322''$ from the X-ray peak. The two X-ray surface brightness profiles are presented in Figure 15. Using the three-component model described in Section 3.2, we detect an X-ray surface brightness edge ($j_n = 1.15 \pm 0.23$) at $231.5 \pm 29.4''$ for the sector scanning from 233° to 263° . In the sector covering 263° to 293° , the density contrast is slightly more prominent ($j_{n_e} = 1.22 \pm 0.07$) and the surface brightness edge positions at $237.1 \pm 6.5''$. To directly compare with Ghizzardi et al. (2014), in which they conducted only projected spectral analysis, we also carry out the projected spectral analysis and infer that the thermal pressure contrasts j_p across the outer X-ray surface brightness edges r_{out} are 0.87 ± 0.19 in the sector covering $233^\circ \leq \phi < 263^\circ$ and $1.17^{+0.11}_{-0.10}$ in the sector covering $263^\circ \leq \phi < 293^\circ$. The mean thermal contrast of these sectors differs from the pressure contrast measured in Ghizzardi et al. (2014) by approximately 1.5σ , showing no statistically significant discrepancy.

A2029

In order to investigate the impact of the curvature-based sector definition in A2029, we analyze a sector region aligned with the most clearly visible spiral excess in the east of the residual X-ray surface brightness map. This sector centers at (15:10:55.8166, 5:44:53.451),

Table 5. A summary of the outer boundaries of the radial bins. (The boundaries are in units of " and measured from the cluster center.)

Cluster	Radial bin	Sector 4 $23^\circ \leq \phi < 53^\circ$	Sector 5 $53^\circ \leq \phi < 83^\circ$	Sector 6 $83^\circ \leq \phi < 113^\circ$	Sector 7 $113^\circ \leq \phi < 143^\circ$	Sector 8 $143^\circ \leq \phi < 173^\circ$	Sector 9 $173^\circ \leq \phi < 203^\circ$	Sector 10 $203^\circ \leq \phi < 233^\circ$	Sector 11 $233^\circ \leq \phi < 263^\circ$	Sector 12 $263^\circ \leq \phi < 293^\circ$	Sector 1 $293^\circ \leq \phi < 323^\circ$	Sector 2 $323^\circ \leq \phi < 353^\circ$	Sector 3 $353^\circ \leq \phi < 383^\circ$		
A496	1	17.000	15.000	17.000	15.000	13.000	15.000	16.000	19.000	19.000	17.000	17.000	16.000		
	2	28.000	25.054	28.691	24.000	21.000	25.628	26.478	34.125	31.000	26.000	27.000	25.000		
	3	38.000	35.000	39.000	33.000	30.224	41.000	40.000	49.000	45.235	35.000	37.000	34.000		
	4	48.000	44.000	48.000	43.000	43.000	56.000	54.000	64.000	61.000	45.131	47.000	42.558		
	5	58.280	52.000	57.000	51.848	56.000	72.000	69.000	78.000	76.000	61.000	58.137	52.000		
	6	74.000	61.000	66.000	62.000	69.000	88.000	82.000	91.000	91.000	79.000	74.000	64.000		
	7	92.340	70.000	75.000	72.000	82.000	105.000	96.000	104.000	105.000	95.000	91.000	79.000		
	8	115.000	79.000	84.000	82.000	96.000	122.396	109.000	117.000	119.000	112.000	109.000	97.602		
	9	137.000	91.512	96.851	93.000	111.000	140.000	123.000	130.000	133.000	129.000	128.000	119.000		
	10	160.000	112.000	115.000	104.000	129.189	159.000	137.000	144.000	147.000	147.000	148.000	139.000		
	11	184.000	134.000	135.000	117.360	150.000	179.000	153.471	158.000	161.000	164.590	169.000	161.000		
	12	214.000	156.000	156.000	136.000	172.000	201.000	170.000	172.000	176.000	182.000	192.000	183.000		
	13	252.000	180.000	177.000	156.000	196.000	225.000	188.000	187.000	192.000	202.000	215.872	205.000		
	14	217.000	198.000	178.000	222.000	207.000	203.000	203.000	208.000	224.000	252.000	227.000			
	15	252.000	222.000	201.000	252.000	229.000	220.000	220.000	226.000	252.000	247.726				
	16		252.000	225.000		252.000		239.185		252.000					
	17			252.000					252.000						
Cluster	Radial bin	Sector 1 $23^\circ \leq \phi < 53^\circ$	Sector 2 $53^\circ \leq \phi < 83^\circ$	Sector 3 $83^\circ \leq \phi < 113^\circ$	Sector 4 $113^\circ \leq \phi < 143^\circ$	Sector 5 $143^\circ \leq \phi < 173^\circ$	Sector 6 $173^\circ \leq \phi < 203^\circ$	Sector 7 $203^\circ \leq \phi < 233^\circ$	Sector 8 $233^\circ \leq \phi < 263^\circ$	Sector 9 $263^\circ \leq \phi < 293^\circ$	Sector 10 $293^\circ \leq \phi < 323^\circ$	Sector 11 $323^\circ \leq \phi < 353^\circ$	Sector 12 $353^\circ \leq \phi < 383^\circ$		
A2029	1	10.000	9.000	8.000	9.753	9.893	11.000	11.000	10.000	10.000	10.000	10.000	9.000		
	2	18.000	16.000	14.170	16.000	17.000	18.000	17.000	16.000	16.000	16.000	17.000	16.000		
	3	25.519	21.291	20.000	22.000	22.000	23.284	23.031	21.000	22.582	21.221	24.000	23.080		
	4	32.000	27.000	25.000	27.000	27.000	29.000	29.000	26.000	28.000	27.000	31.230	31.000		
	5	38.000	33.000	30.000	31.000	32.000	35.000	36.000	32.000	34.000	33.000	38.000	39.000		
	6	45.000	39.000	35.000	36.000	37.841	42.000	43.000	38.000	40.000	39.000	44.000	47.000		
	7	52.000	44.000	40.000	41.000	44.000	50.000	51.000	44.000	46.000	45.000	51.000	55.000		
	8	59.000	50.000	45.000	46.000	51.000	59.000	60.000	51.000	52.000	51.000	58.000	63.000		
	9	66.268	56.000	50.000	50.678	58.000	67.889	70.000	58.000	58.000	57.000	65.000	72.000		
	10	75.000	62.000	55.000	56.000	67.000	79.000	81.000	66.000	65.000	63.000	73.000	80.770		
	11	84.000	68.390	60.326	61.000	76.000	91.000	94.000	74.000	72.000	70.000	81.000	92.000		
	12	95.000	75.000	66.000	67.000	86.000	106.000	108.834	83.000	80.000	77.000	90.000	104.000		
	13	107.000	83.000	72.000	73.000	98.000	122.000	125.000	93.000	89.000	84.000	99.000	118.000		
	14	121.000	92.000	78.000	80.000	112.000	141.000	143.000	105.000	97.000	91.000	109.000	134.000		
	15	138.000	103.000	85.000	88.000	127.000	163.000	164.000	119.722	105.000	98.000	120.000	153.000		
	16	157.000	115.000	92.000	97.000	144.000	186.000	187.000	133.000	114.000	106.000	130.121	177.000		
	17	179.000	129.000	100.000	106.000	163.000	213.000	214.000	147.000	123.000	114.000	142.000	206.000		
	18	206.000	144.000	109.000	116.000	185.000	242.000	242.000	162.000	132.000	122.000	156.000	242.000		
	19	242.000	161.000	119.000	127.000	213.000									
	20	181.000	130.000	139.000	242.000										
	21	207.000	142.000	152.000											
	22	242.000	155.000	167.000											
	23		169.000	192.000											
	24		189.000	217.000											
	25		216.000	242.000											
	26		242.000												
	27														
Cluster	Radial bin	Sector 11 $28^\circ \leq \phi < 58^\circ$	Sector 12 $58^\circ \leq \phi < 88^\circ$	Sector 1 $88^\circ \leq \phi < 118^\circ$	Sector 2 $118^\circ \leq \phi < 148^\circ$	Sector 3 $148^\circ \leq \phi < 178^\circ$	Sector 4 $178^\circ \leq \phi < 208^\circ$	Sector 5 $208^\circ \leq \phi < 238^\circ$	Sector 6 $238^\circ \leq \phi < 268^\circ$	Sector 7 $268^\circ \leq \phi < 298^\circ$	Sector 8 $298^\circ \leq \phi < 328^\circ$	Sector 9 $328^\circ \leq \phi < 358^\circ$	Sector 10 $358^\circ \leq \phi < 388^\circ$		
A1644	1	20.000	25.364	19.862	16.052	20.121	15.000	14.000	17.000	16.648	15.000	19.000	22.000		
	2	33.630	42.610	91.000	93.000	92.000	26.956	22.000	27.000	26.000	25.392	32.255	37.498		
	3	45.000	94.000	142.000	141.000	137.000	107.000	32.047	35.656	33.000	36.077	42.000	45.000		
	4	54.000	143.000	184.000	182.000	179.000	163.000	112.000	95.000	40.105	77.000	49.000	51.000		
	5	63.000	184.000	222.000	222.000	222.000	164.000	140.000	102.000	124.000	55.000	56.501			
	6	71.095	222.000				222.000	180.000	155.000	174.000	61.000	79.000			
	7	105.000						222.000	222.000	222.000	66.082	106.000			
	8	143.000									93.000	140.000			
	9	181.000										120.000	178.000		
	10	222.000										150.000	222.000		
	11											182.000			
	12											222.000			

^aThe radial bins are counted from the cluster center.

scans from 160° to 240° , and extends from $2''$ to $242''$.

Table 7. Summary of the tied radial bins in A1644.

Cluster	Sector	Tied Radial bins ^a
A1644	7	$(2^{\text{nd}}, 3^{\text{rd}})$
	8	$(1^{\text{st}}, 2^{\text{nd}})$
	9	$(3^{\text{rd}}, 4^{\text{th}}, 5^{\text{th}}, 6^{\text{th}})$
	10	$(1^{\text{st}}, 2^{\text{nd}}), (3^{\text{rd}}, 4^{\text{th}}, 5^{\text{th}})$
	11	$(1^{\text{st}}, 2^{\text{nd}}), (3^{\text{rd}}, 4^{\text{th}})$

^aThe radial bins listed in parentheses are tied together.

Through modeling the X-ray surface brightness profile (Figure 16) of this sector with the three-component density model expressed in Equation 1, we measure a subtle density contrast $j_n = 1.023 \pm 0.01654$ at $r_{\text{out}} = 32.5 \pm 0.8''$. The density contrast of this curvature-based sector is marginally greater than 1, in contrast to the

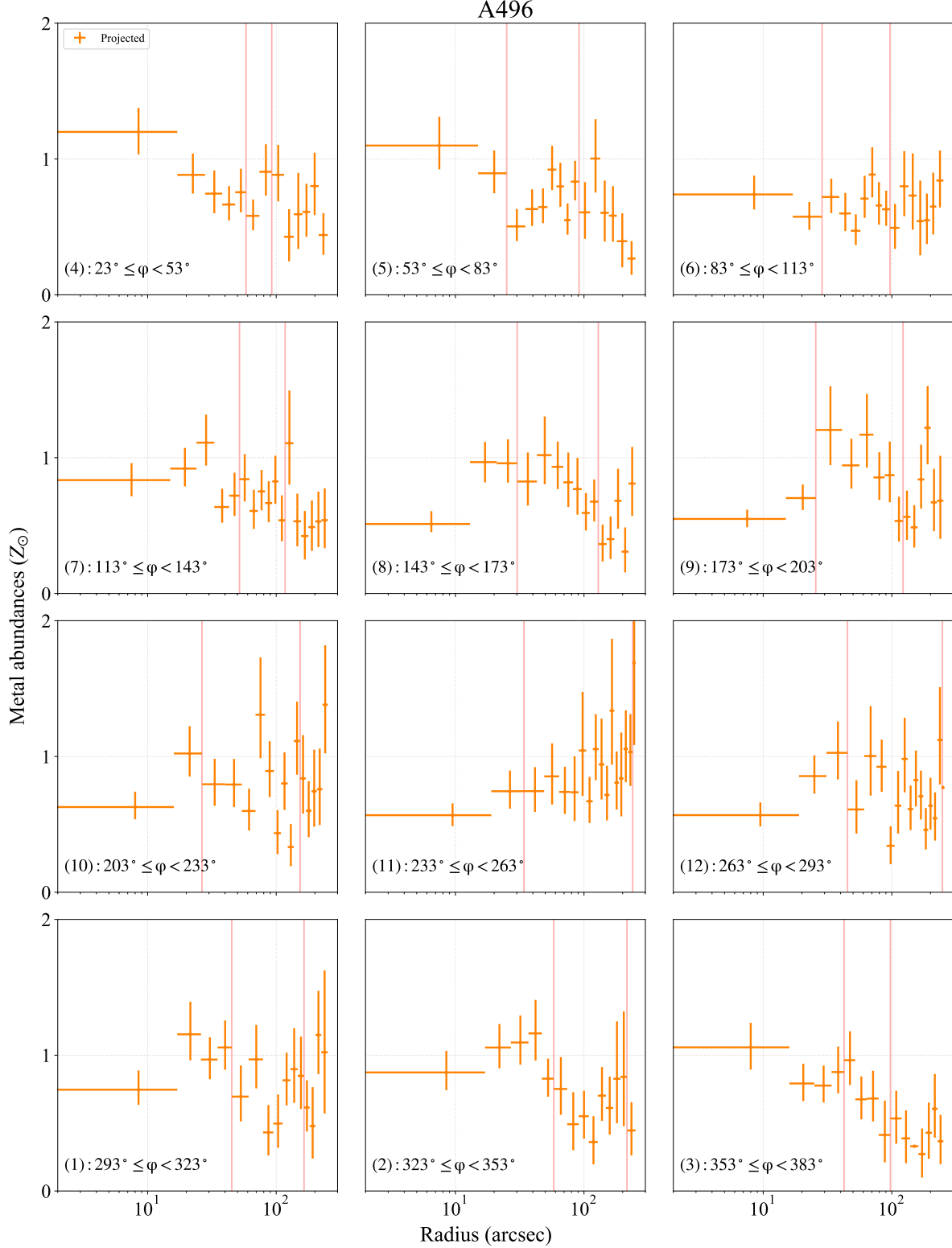


Figure 12. Radial ICM metal abundance profiles of each sector in A496. The orange data points show the projected metal abundances. The horizontal bars represent the ranges of the radial bins and the vertical bars denote the 1σ confidence range of the metal abundance. The pink vertical lines show the positions of r_{in} and r_{out} described in Section 3.2.

density contrasts of the edges detected in the default

analysis: as seen in Section 3.2, r_{in} of the sector 7 and

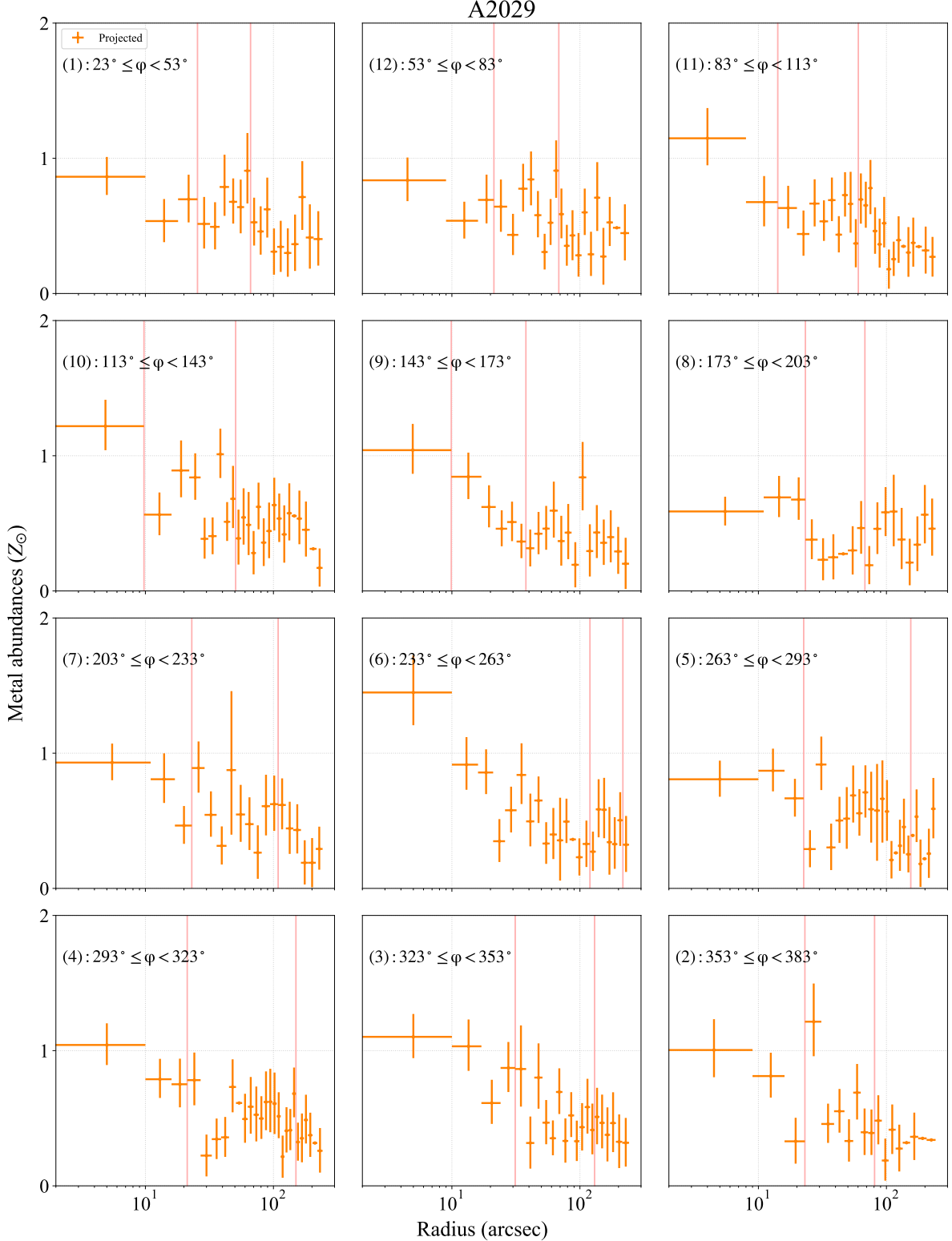


Figure 13. Same as Figure 12, but for A2029.

8, and r_{out} of the sector 9, which roughly cover the same region, have density contrasts below 1. The density

contrast measured in the curvature-based sector differs from the mean value of those sectors by 2.2σ , indicat-

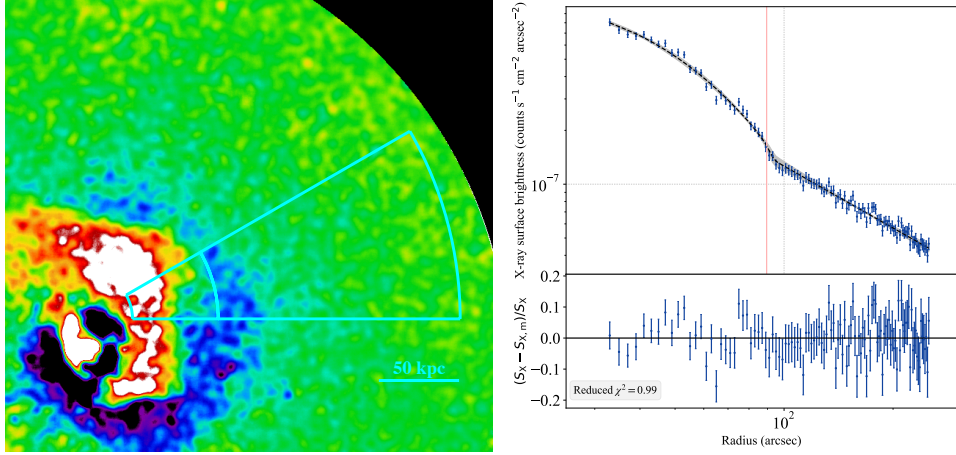


Figure 14. The residual X-ray surface brightness map of the northwestern region of A496 (left) and the X-ray surface brightness profile (right) extracted from the region enclosed by the cyan sector shown in the left panel. (Left): the cyan sector is aligned with the curvature of the spiral excess, as described in Section C, and the cyan arc shows the position of the detected edge determined from the X-ray surface brightness fitting. The horizontal bar denotes the spatial scale. (Right): same format as in Figure 3.

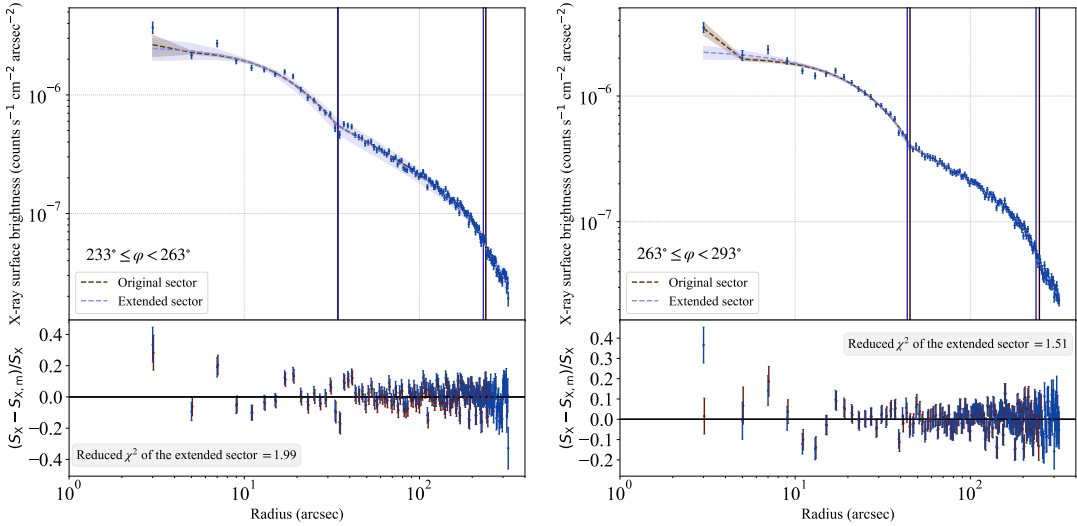


Figure 15. The X-ray surface brightness profiles extracted from sectors of $233^\circ \leq \phi < 263^\circ$ (left) and $263^\circ \leq \phi < 293^\circ$ (right) in A496, as described in Section C. The outer boundaries of these sectors are extended to $322''$ to allow a more accurate determination of the edge r_{out} . Same format and symbols as used in Figure 3. The brown dashed line and vertical lines indicate the best-fit profile and the edges positions obtained from the original sector, which covers the same azimuthal range with the extended sector but adopts a smaller outer boundary ($252''$). The brown and blue data points in the lower panel show the corresponding residuals from the original and extended sectors, respectively.

ing a moderate discrepancy. Additionally, we perform the deprojected spectral analysis of the curvature-based sector to determine whether cold front exists. Following the method described in Section 3.3, but increasing the mean photon counts in each radial bin to 4534 per bin, we measure the temperature contrast to be $0.4379^{+0.0770}_{-0.0443}$, which is in disagreement with our default analysis. Thus, we detect a cold front in this curvature-based sector according to our cold front criteria. This

finding indicates that, when the density contrast is subtle, carefully defining the sector could play a role in identifying cold fronts. Since the sectors defined in Section 3.2 have smaller opening angles, they are better suited to capture the azimuthal variation in cold front properties.

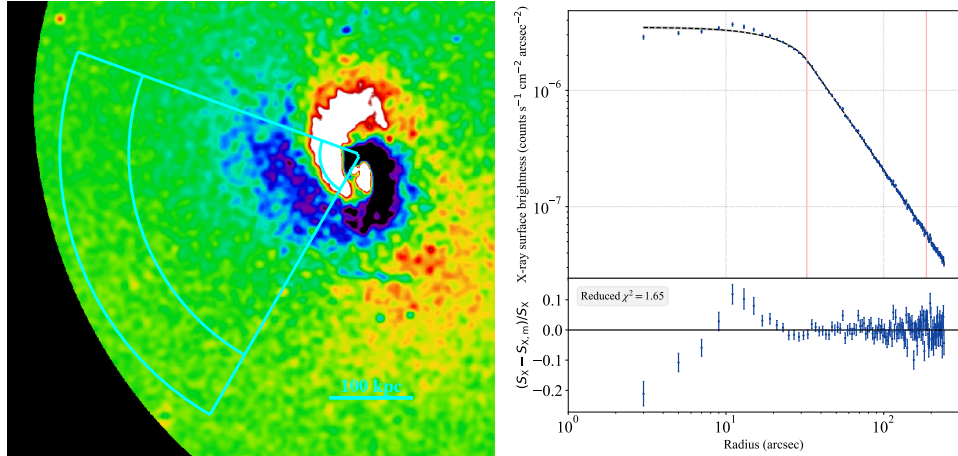


Figure 16. The residual X-ray surface brightness map of the eastern region of A2029 (left) and the X-ray surface brightness profile (right) extracted from the region enclosed by the cyan sector shown in the left panel. (Left): the cyan sector is aligned with the curvature of the spiral excess, as described in Section C, and the cyan arc shows the position of the detected edge determined from the X-ray surface brightness fitting. The horizontal bar denotes the spatial scale. (Right): same format as in Figure 3.

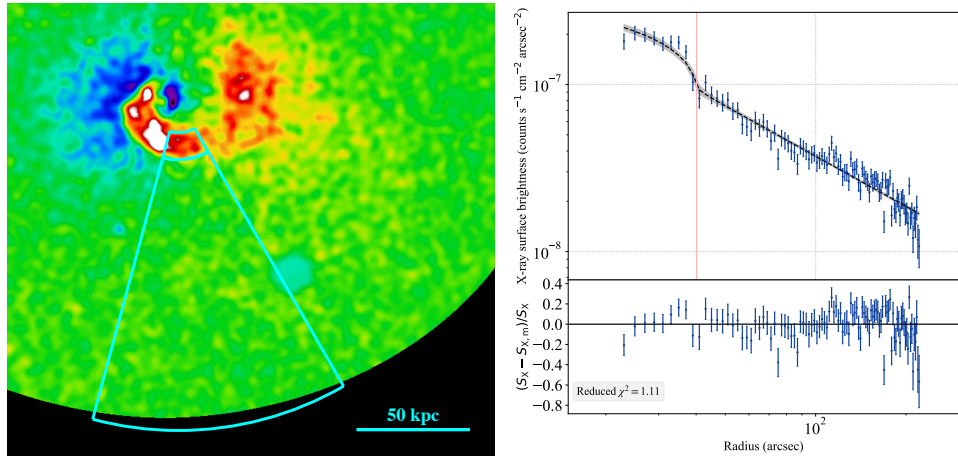


Figure 17. The residual X-ray surface brightness map of the southern region of A1644 (left) and the X-ray surface brightness profile (right) extracted from the region enclosed by the cyan sector shown in the left panel. (Left): the cyan sector is aligned with the curvature of the spiral excess, as described in Section C, and the cyan arc shows the position of the detected edge determined from the X-ray surface brightness fitting. The horizontal bar denotes the spatial scale. (Right): same format as in Figure 3.

A1644

We analyze a sector aligned with the spiral excess in the residual X-ray surface brightness map for A1644. The sector is centered at $(12:57:10.7043, -17:24:33.480)$ and spans an azimuthal angle from 255° to 300° with an open angle of 45° . We extract the X-ray surface brightness profile within this sector over the radial range $22'' - 222''$ (Figure 17), and fit it using the two-component density model described in Section 3.2. The reason we switch from the three-component density model to the two-component density model for fitting

this sector is that r_{in} of the sector 7 in the same direction described in Section 3.2 appears to align with the inner edge of the spiral excess. However, the curvature-based sector used here starts from the middle of the spiral excess and does not include the inner-edge region. Therefore, we expect that only one edge remains within this curvature-based sector. The density contrasts j_n of the sector 7 defined in Section 3.2 and the curvature-based sector, 2.110 ± 0.1554 and 1.563 ± 0.1459 respectively, differ by $\approx 2.57\sigma$. Meanwhile, the density contrast in the curvature-based sector is lower than in the sector defined in Section 3.2. Such a reduction may result from

the broader opening angle of the curvature-based sector,

which has the potential to either smear out or amplify the density contrasts.

REFERENCES

- Arnaud, K. A. 1996, in Astronomical Society of the Pacific Conference Series, Vol. 101, Astronomical Data Analysis Software and Systems V, ed. G. H. Jacoby & J. Barnes, 17
- Ascasibar, Y., & Markevitch, M. 2006, *ApJ*, 650, 102
- Astropy Collaboration, Robitaille, T. P., Tollerud, E. J., et al. 2013, *A&A*, 558, A33
- Blanton, E. L., Randall, S. W., Clarke, T. E., et al. 2011, *ApJ*, 737, 99
- Chen, H., Jones, C., Andrade-Santos, F., ZuHone, J. A., & Li, Z. 2017, *ApJ*, 838, 38
- Chibueze, J. O., Sakemi, H., Ohmura, T., et al. 2021, *Nature*, 593, 47
- Churazov, E., Forman, W., Jones, C., & Böhringer, H. 2003, *ApJ*, 590, 225
- Clarke, T. E., Blanton, E. L., & Sarazin, C. L. 2004a, *ApJ*, 616, 178
- Clarke, T. E., Uson, J. M., Sarazin, C. L., & Blanton, E. L. 2004b, *ApJ*, 601, 798
- Dupke, R., & White, III, R. E. 2003, *ApJL*, 583, L13
- Dupke, R., White, III, R. E., & Bregman, J. N. 2007, *ApJ*, 671, 181
- Erdim, M. K., & Hudaverdi, M. 2019, *MNRAS*, 488, 2917
- Foreman-Mackey, D., Hogg, D. W., Lang, D., & Goodman, J. 2013, *PASP*, 125, 306
- Foster, A., Chakraborty, P., Okon, H., et al. 2023, in American Astronomical Society Meeting Abstracts, Vol. 242, American Astronomical Society Meeting Abstracts, 318.02
- Foster, A. R., Ji, L., Smith, R. K., & Brickhouse, N. S. 2012, *ApJ*, 756, 128
- Fruscione, A., McDowell, J. C., Allen, G. E., et al. 2006, in Society of Photo-Optical Instrumentation Engineers (SPIE) Conference Series, Vol. 6270, Observatory Operations: Strategies, Processes, and Systems, ed. D. R. Silva & R. E. Doxsey, 62701V
- Garmire, G. P., Bautz, M. W., Ford, P. G., Nousek, J. A., & Ricker, Jr., G. R. 2003, in Society of Photo-Optical Instrumentation Engineers (SPIE) Conference Series, Vol. 4851, X-Ray and Gamma-Ray Telescopes and Instruments for Astronomy., ed. J. E. Truemper & H. D. Tananbaum, 28–44
- Gatuzz, E., Sanders, J. S., Canning, R., et al. 2022, *MNRAS*, 513, 1932
- Ghizzardi, S., De Grandi, S., & Molendi, S. 2014, *A&A*, 570, A117
- Goodman, J., & Weare, J. 2010, *Communications in Applied Mathematics and Computational Science*, 5, 65
- Grant, C. E., Bautz, M. W., Plucinsky, P. P., & Ford, P. G. 2024, in Society of Photo-Optical Instrumentation Engineers (SPIE) Conference Series, Vol. 13093, Space Telescopes and Instrumentation 2024: Ultraviolet to Gamma Ray, ed. J.-W. A. den Herder, S. Nikzad, & K. Nakazawa, 130931E
- Hallman, E. J., & Markevitch, M. 2004, *ApJL*, 610, L81
- HI4PI Collaboration, Ben Bekhti, N., Flöer, L., et al. 2016, *A&A*, 594, A116
- Ichinohe, Y., Simionescu, A., Werner, N., Fabian, A. C., & Takahashi, T. 2019, *MNRAS*, 483, 1744
- Ichinohe, Y., Simionescu, A., Werner, N., Markevitch, M., & Wang, Q. H. S. 2021, *MNRAS*, 504, 2800
- Ichinohe, Y., Simionescu, A., Werner, N., & Takahashi, T. 2017, *MNRAS*, 467, 3662
- Ichinohe, Y., Werner, N., Simionescu, A., et al. 2015, *MNRAS*, 448, 2971
- Johnson, R. E., Markevitch, M., Wegner, G. A., Jones, C., & Forman, W. R. 2010, *ApJ*, 710, 1776
- Kempner, J. C., Sarazin, C. L., & Ricker, P. M. 2002, *ApJ*, 579, 236
- Landau, L. D., & Lifshitz, E. M. 1959, *Fluid mechanics*
- Markevitch, M., & Vikhlinin, A. 2007, *PhR*, 443, 1
- Markevitch, M., Vikhlinin, A., & Mazzotta, P. 2001, *ApJL*, 562, L153
- Markevitch, M., Ponman, T. J., Nulsen, P. E. J., et al. 2000, *ApJ*, 541, 542
- Monteiro-Oliveira, R., Doubrava, L., Machado, R. E. G., et al. 2020, *MNRAS*, 495, 2007
- Naor, Y., Keshet, U., Wang, Q. H. S., & Reiss, I. 2020, *MNRAS*, 495, 4392
- Paterno-Mahler, R., Blanton, E. L., Randall, S. W., & Clarke, T. E. 2013, *ApJ*, 773, 114
- Reiprich, T. H., & Böhringer, H. 2002, *ApJ*, 567, 716
- Reiprich, T. H., Sarazin, C. L., Kempner, J. C., & Tittley, E. 2004, *ApJ*, 608, 179
- Roediger, E., Brüggen, M., Simionescu, A., et al. 2011, *MNRAS*, 413, 2057
- Roediger, E., Kraft, R. P., Forman, W. R., Nulsen, P. E. J., & Churazov, E. 2013, *ApJ*, 764, 60

- Roediger, E., Lovisari, L., Dupke, R., et al. 2012, MNRAS, 420, 3632
- Rossetti, M., Ghizzardi, S., Molendi, S., & Finoguenov, A. 2007, A&A, 463, 839
- Smith, R. K., Brickhouse, N. S., Liedahl, D. A., & Raymond, J. C. 2001, ApJL, 556, L91
- Tanaka, T., Kunieda, H., Hudaverdi, M., Furuzawa, A., & Tawara, Y. 2006, PASJ, 58, 703
- Tashiro, M., Watanabe, S., Maejima, H., et al. 2024, in Society of Photo-Optical Instrumentation Engineers (SPIE) Conference Series, Vol. 13093, Space Telescopes and Instrumentation 2024: Ultraviolet to Gamma Ray, ed. J.-W. A. den Herder, S. Nikzad, & K. Nakazawa, 130931G
- Ueda, S., & Ichinohe, Y. 2024, ApJ, 973, 98
- Ueda, S., Kitayama, T., & Dotani, T. 2017, ApJ, 837, 34
- Ueda, S., Umetsu, K., Ng, F., et al. 2021, ApJ, 922, 81
- Vikhlinin, A., Markevitch, M., & Murray, S. S. 2001, ApJ, 551, 160
- Walker, S. A., Hlavacek-Larrondo, J., Gendron-Marsolais, M., et al. 2017, MNRAS, 468, 2506
- ZuHone, J. A. 2011, ApJ, 728, 54
- ZuHone, J. A., Markevitch, M., Brunetti, G., & Giacintucci, S. 2013, ApJ, 762, 78
- ZuHone, J. A., Markevitch, M., & Johnson, R. E. 2010, ApJ, 717, 908